# Quantum-state Selective Nuclear Decay Spectroscopy

Lorenz, Ch.

2018

*Document Version:*
Publisher's PDF, also known as Version of record

# Quantum-state Selective Nuclear Decay Spectroscopy

CHRISTIAN LORENZ
FACULTY OF SCIENCE | LUND UNIVERSITY 2019

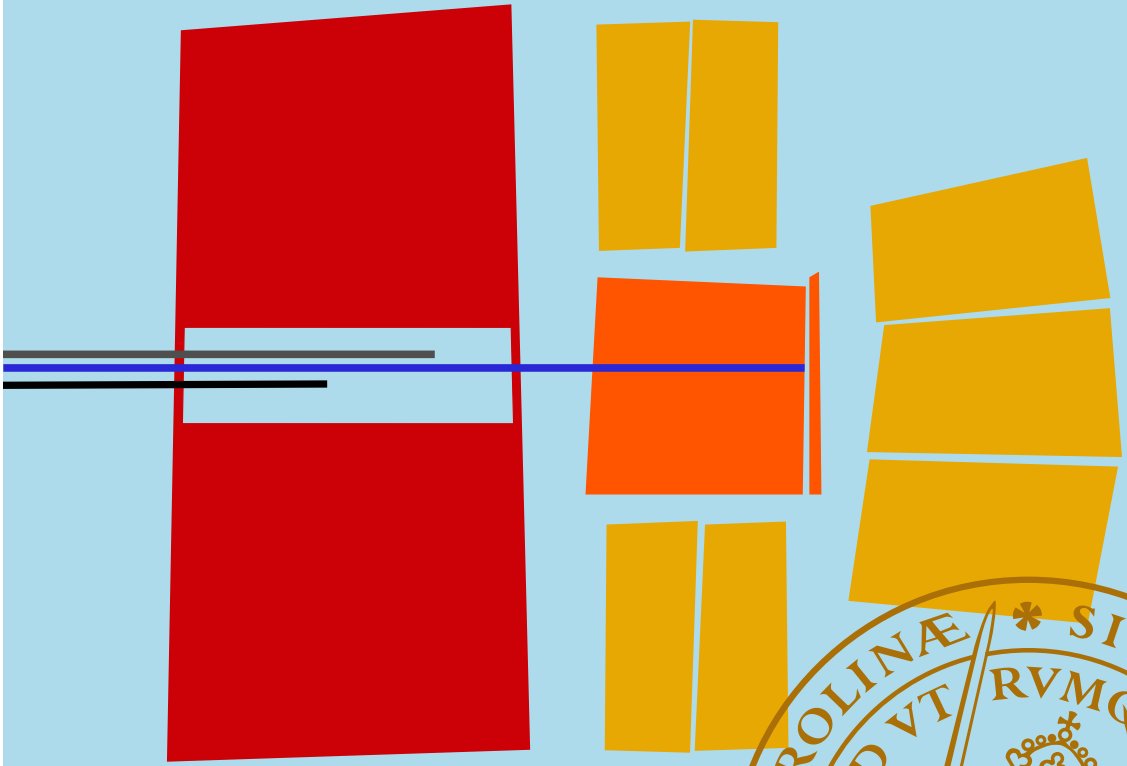

# Quantum-state Selective Nuclear Decay Spectroscopy

by Christian Lorenz


LUND
UNIVERSITY

Dissertation for the degree of
Doctor of Philosophy

Thesis advisors: Prof. Dirk Rudolph,
Dr. Pavel Golubev, Dr. Luis G. Sarmiento Pico

Faculty opponent: Dr. Augusto O. Macchiavelli

Academic dissertation which, by due permission of the Faculty of Science at Lund University, will be publicly defended on Friday, January 25th, 2019 at 13:15 in the Rydberg lecture hall (Rydbergsalen) at the Department of Physics, Sölvegatan 14A, Lund, for the degree of Doctor of Philosophy.

Organization
**LUND UNIVERSITY**

Department of Physics
Division of Nuclear Physics
Box 118, SE–221 00 LUND
Sweden

Document name
**DOCTORAL DISSERTATION**

Date of disputation
2019-01-25

Sponsoring organization

Author(s)
Christian Lorenz

Title
Quantum-state Selective Nuclear Decay Spectroscopy

Abstract

This thesis focusses on the results of two experiments employing Penning traps to prepare pure beams of the $^{213}$Ra ground state and $^{127}$Cd, which were then studied with the decay-spectroscopy setup TASISpec. The experiments were conducted with SHIPTRAP at the GSI Helmholtzzentrum für Schwerionenforschung in Darmstadt, Germany, and JYFLTRAP at the IGISOL Accelerator Facility at the University of Jyväskylä, Finland.

The $\alpha$-decay branching ratios of the $^{213}$Ra ground state have been revised based on comprehensive GEANT4 simulations, i.e. 'virtual experiments', which were confronted with the experimental results. These findings are supported by theoretical calculations. This work is published in Papers I and II. Using the same method, the proton-decay branch of the $^{53}$Co 3174 keV isomer has been studied, which is the content of Paper IV.

In Paper III the results of the $^{127}$Cd experiment are presented. There the decay scheme of $^{127}$In populated by the $\beta$ decay of $^{127}$Cd was considerably extended and the $\beta$ feeding into the individual states deduced. Extensive shell-model calculations have been conducted to calculate the energy levels and $\gamma$-ray branching ratios of $^{127}$In as well as the Gamow-Teller strength distributions of the $\beta$ decay of the $3/2^+$ and $11/2^-$ states in $^{127}$Cd. Based on these calculations the experimentally observed decay-scheme of $^{127}$In could be reproduced remarkably well. The order of the $3/2^+$ and $11/2^-$ state in $^{127}$Cd has been established, identifying the $3/2^+$ state as the ground state and the $11/2^-$ state as the 283 keV isomer. Furthermore, the phase-depended cleaning method was employed for the first time in an attempt to study the $\beta$ decay of the $^{127}$Cd isomer individually.



Key words
nuclear structure, alpha decay, beta decay, gamma rays, spectroscopy, Penning traps, shell-model calculations, GEANT4 Monte Carlo Simulations

Classification system and/or index terms (if any)

Supplementary bibliographical information

Language
English

ISSN and key title
LUNFD6/(NFFR-1043)/1-75(2018)

ISBN
978-91-7753-942-1 (print)
978-91-7753-943-8 (pdf)

Recipient's notes

Number of pages
147

Price

Security classification

Distribution by Christian Lorenz, Division of Nuclear Physics, Lund University, Box 118, SE–221 00 LUND.



Signature 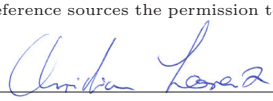 Date 2018-12-10

# Quantum-state Selective Nuclear Decay Spectroscopy

by Christian Lorenz


LUND
UNIVERSITY

A doctoral thesis at a university in Sweden takes either the form of a single, cohesive research study (monograph) or a summary of research papers (compilation thesis), which the doctoral student has written alone or together with one or several other author(s).

In the latter case the thesis consists of two parts. An introductory text puts the research work into context and summarizes the main points of the papers. Then, the research publications themselves are reproduced, together with a description of the individual contributions of the authors. The research papers may either have been already published or are manuscripts at various stages (in press, submitted, or in draft).

**Cover illustration:** Designed by Nataša Lalović.

**Funding information:** This work is supported by the Knut and Alice Wallenberg foundation (KAW 2015.0021) and the Swedish Research Council (VR 2013-4271).



Faculty of Science, Department of Physics

ISBN: 978-91-7753-942-1 (print)
ISBN: 978-91-7753-943-8 (pdf)
ISSN: LUNFD6/(NFFR-1043)/1-75(2019)

Printed in Sweden by Media-Tryck, Lund University, Lund 2019

*Meinen Großeltern*

# Contents

# List of publications and author's contributions

## Paper I

**Geant4-aided Quantum State Selective Decay Spectroscopy of $^{213}$Ra**
(PoS, Adelaide, 2016), **INPC2016**, 073
**Ch. Lorenz**, L.G. Sarmiento, D. Rudolph, and M. Block

I prepared and performed the simulations, developed the routine presented in the paper and wrote the paper.

## Paper II

**Quantum-state-selective decay spectroscopy of $^{213}$Ra**
Phys. Rev. C **96**, 034315 (2017).
**Ch. Lorenz**, L.G. Sarmiento, D. Rudolph, D.E. Ward, M. Block, F.P. Heßberger, D. Ackermann, L.-L. Andersson, M.L. Cortés, C. Droese, M. Dworschak, M. Eibach, U. Forsberg, P. Golubev, R. Hoischen, I. Kojouharov, J. Khuyagbaatar, D. Nesterenko, I. Ragnarsson, H. Schaffner, L. Schweikhard, S. Stolze, and J. Wenzl

I finalized the routine presented in Paper I, carried out the analysis and comparison of simulation and experiment, wrote the majority of the manuscript and was responsible for editing the manuscript.

## Paper III

**$\beta$ decay of $^{127}$Cd and excited states in $^{127}$In**
Phys. Rev. C, submitted.
**Ch. Lorenz**, L.G. Sarmiento, D. Rudolph, T. Eronen, A. Kankainen, D.A. Nesterenko, L. Canete, A. Fernandez, U. Forsberg, P. Golubev, A. Jungclaus, I. Kojouharov, N. Lalović, J. Partanen, M. Reponen, S. Rinta-Antila, A. de Roubin, V. Vaquero, M. Vilén

I was actively involved in preparing the experiment as well as coordinated and set up the experiment on site. Together with L. G. Sarmiento I took the main responsibility for conducting the experiment and taking shifts. I calibrated and analysed the obtained data in all aspects and performed the shell-model calculations. I wrote the manuscript and was responsible for editing the manuscript.

## Paper IV

**Quantum-state Selective Decay Spectroscopy: The Proton Branch of $^{53}$Co$^{m}$**

Phys. Rev. Lett., to be submitted.

L.G. Sarmiento, **Ch. Lorenz**, D. Rudolph, C. Fahlander, P. Golubev, U. Forsberg, N. Lalović, A. Kankainen, L. Canete, D. Cox, T. Eronen, J. Hakala, A. Jokinen, V. Kolhinen, J. Koponen, I. Moore, P. Papadakis, I. Pohjalainen, J. Reinikainen, S. Rinta-Antila, A. Voss, M. Block, J. Gerl, I. Kojouharov, N. Kurz, H. Schaffner, and T. Habermann

I was actively involved in preparing and setting up the experiment as well as conducting the experiment and taking shifts. I was responsible for the calibration of the obtained $\gamma$-ray data.

# Publications not included in this thesis

**Upgrade and Commissioning of the Lund-York-Cologne CAlorimeter**
GSI Scientific Report 2016 **2017-1**, 190 (2017).
B. Fu, K. Wolf, P. Reiter, M.A. Bentley, P. J. Coleman-Smith, S. Fox, C. Goergen, P. Golubev, I. Lazarus, **C. Lorenz**, D. Rudolph, L. Scruton, and S. Thiel

**Recent upgrades of the SHIPTRAP setup: On the finish line towards direct mass spectroscopy of superheavy elements**
Acta Phys. Pol. B **48**, 423 (2017).
F. Giacoppo, K. Blaum, M. Block, P. Chhetri, Ch.E. Düllmann, C. Droese, S. Eliseev, P. Filianin, S. Götz, Y. Gusev, F. Herfurth, F.P. Heßberger, O. Kaleja, J. Khuyagbaatar, M. Laatiaoui, F. Lautenschläger, **C. Lorenz**, G. Marx, E. Minaya Ramirez, A. Mistry, Yu.N. Novikov, W.R. Plass, S. Raeder, D. Rodríguez, D. Rudolph, L.G. Sarmiento, C. Scheidenberger, L. Schweikhard, P. Thirolf, A. Yakushev

**High-precision mass measurements for the isobaric multiplet mass equation at A = 52**
J. Phys. G: Nucl. Part. Phys. **44**, 065103 (2017).
D. A. Nesterenko, A. Kankainen, L. Canete, M. Block, D. Cox, T. Eronen, C. Fahlander, U. Forsberg, J. Gerl, P. Golubev, J. Hakala, A. Jokinen, V.S. Kolhinen, J. Koponen, N. Lalović, **Ch. Lorenz**, I.D. Moore, P. Papadakis, J. Reinikainen, S. Rinta-Antila, D. Rudolph, L.G. Sarmiento, A. Voss, and J. Äystö

# Acknowledgements

Of course, this work would not have been possible without help and support of many people:
My supervisor Dirk. Thank you for your guidance, your support and for always having a plan B. Although having enough workload otherwise, your door remained open for humble questions and discussions at all times.
Pavel. Thank you for getting me hands-on gluing, screwing, soldering, cutting, ..., all kinds of bits and pieces to finally produce a functioning detector device. Your company on so many road trips and cosy nights in Hotel Elite made those trips a joy.
Pico. Thank you for all your help when it comes to GEANT4 and other IT related issues, for your patience when poking you with questions of all sorts, and, of course, for making that DAQ work.
Ulrika. Moving to and around Lund would not have been possible without you. Thank you for all your support as friend and colleague.
Johan. Thank you for your reliable and eager dedication on the badminton field, helping me to get my physical counterbalance to my office chair. Some day we will defeat Pontus.
Anneli. Thank you for getting us started and into the system so quickly and smoothly.
Charlotta. Teaching could not have been a more organized experience.
Thank you to Johan, Linus, Vitenys, Alexander and Maria for creating a calm and nice office atmosphere.
Rasmus and Frida, our work-unrelated outpost.

Nicht zuletzt gebührt mein Dank:
Meinen Eltern Babara und Frank. Ohne euch und eure endlose Unterstützung wäre all das nicht möglich gewesen. Meiner Dankbarkeit für Rat und Tat zu jeder Zeit können Worte wohl nur mäßig Ausdruck verleihen.
Meinem Bruder Sebastian, für die zweisame Studienzeit und - vor allem - dafür, mein Bruder zu sein.
Meinen Großeltern Christine und Konrad, die in all den nachmittäglichen Stunden mein mathematisches und physikalischen Hirn (und auch alle anderen) auf den rechten Weg gebracht haben. Auch hier vermag das Vokabular der deutschen Sprache nicht, meiner Dankbarkeit für eure großelterliche Weisheit gerecht zu werden.
I jedno stvarno veliko hvala:
Natašinoj porodici, Milici, Milisavu, Mirjani, Danilu, Žarku i Relji, koji su mene srcem i ljubavlju učinili članom svoje familije kao da sam oduvijek bio sa njima.
Mojoj ženi Nataši. Nema riječi. Ti si moj centar.

# Populärvetenskaplig sammanfattning

Allt som vi ser och arbetar med i vårt vardagliga liv består av atomer. De är mycket små, omkring $10^{-10}$ meter. De syns inte med blotta ögat, utan kräver avancerade elektronmikroskop. Men atomerna själva består av ännu mindre beståndsdelar, ett elektronmoln som kretsar kring en kärna.
Atomkärnan består av neutroner och protoner och är bara cirka $10^{-15}$ meter stor. Neutroner och protoner hålls samman av en stark kraft som faktiskt kallas "starka kraften". Samtidigt har protoner en positiv laddning och stöter därför bort varandra. Beroende av balansen mellan protoner och neutroner i atomkärnan kan de vara stabila eller radioaktiva. Om de är radioaktiva betyder det att de sönderfaller efter en viss tid. Det finns fler än 3000 kända kombinationer av protoner och neutroner, "isotoper", som har en livstid längre än $10^{-7}$ sekunder. Men endast 253 av dessa är stabila. Om kärnan inte är helt stabil, sönderfaller den genom utsändning av protoner, neutroner, $\alpha$ partiklar (heliumkärnor), $\beta$-strålning eller genom fission. En atomkärna kan också vara i ett exciterad tillstånd. Oftast de-exciteras de till grundtillståndet genom att sända ut fotoner som kallas $\gamma$-strålning. Detekterar och analyserar man strålningen kan man fastställa kärnans struktur. Resultat från ett sådant experiment används sedan för att förbättra de teorier som beskriver den underliggande kraft som håller samman atomkärnor.
Eftersom de flesta av de intressanta isotoperna inte finns i naturen samt har korta livstider måste de framställas artificiellt i laboratoriet med en kärnreaktion. Tyvärr är det ofta inte enbart de intressanta isotoperna som produceras i reaktionen utan de flesta producerade atomkärnor är inte de som man vill studera. Därför måste man separera de intressanta isotoperna från alla andra på något sätt.
Isotoperna som studerades i den här avhandlingen separerades med hjälp av en så kallad "Penning trap". Penningfällor är de mest precisa maskiner som finns för att mäta kärnors massa. Eftersom alla olika isotoper har olika massor, är Penningfällor mycket precisa för att selektera de önskade atomerna. Under vissa omständigheter kan de även selektera ett visst tillstånd hos en isotop. Detta utnyttjades för att studera sönderfallen av $^{213}$Ra och $^{127}$Cd. Vid analysen av $^{213}$Ra-experimentet jämfördes resultatet med detaljerade simuleringar av hela sönderfalls- och detektionsprocessen, där renheten av $^{213}$Ra-strålen i experimentet blev grundförutsättningen för att få en precis och meningsfull simulering. Vid ett andra experiment sönderföll $^{127}$Cd till $^{127}$In. Analysen av $\gamma$-strålningen resulterade i identifikation av nya energinivåer i $^{127}$In. Dessutom har $^{127}$Cd-sönderfallsprocessen och energinivåer i $^{127}$In beräknats med den sfäriska skalmodellen. Det konstaterades att den teoretiska beskrivningen kunde reproducera de experimentella observationerna mycket väl.

# Chapter 1

# Introduction

Since the discovery of the atomic nucleus in the early $20^{\text{th}}$ century by E. Rutherford [1], a wide range of phenomena have been observed [2, 3]: from nuclear states that come about by single nucleons being excited, to collective excitations such as rotations and vibrations of the nucleus as a whole, nuclei of spherical shape and nuclei that are deformed, nuclei with *magic* proton and neutron numbers, and nuclei with substructures like $\alpha$ clusters [4, 5] or neutron skins [6], to name but a few. Alongside such discoveries and continuous measurements of nuclear properties, theories explaining these findings evolved. Although many theoretical models are in place describing certain phenomena for all, or at least a significant number of nuclei, it remains extremely challenging to formulate a general description addressing all aspects of all nuclear systems, from light nuclei with a handful of nucleons, to heavy and super-heavy nuclei with two or nearly three hundred nucleons. The nuclear chart with over 3000 known isotopes [7] is shown in figure 1.1.

Understanding of nuclear properties has impact on many neighbouring scientific areas, e.g. reactor physics, astrophysics, nuclear medicine, and security. In nuclear reactors, for example, it is crucial to know nuclear decay properties of those nuclei that are produced by nuclear fission, in order to estimate the produced heat or the damage on the reactor vessel caused by neutron, $\beta$ and $\gamma$ radiation. Another example is the astrophysical quest to understand the abundances of all the elements in the universe. The so-called $r$-process is one fundamental piece in solving this quest. One problem is that many nuclei are involved, which neither are naturally present on Earth (because they have lifetimes of the order of milliseconds or even shorter) nor can they be produced by the currently running accelerator facilities. Hence, required nuclear properties, e.g. lifetimes, of nuclei that play a role in the $r$-process have to be inferred from theoretical models.

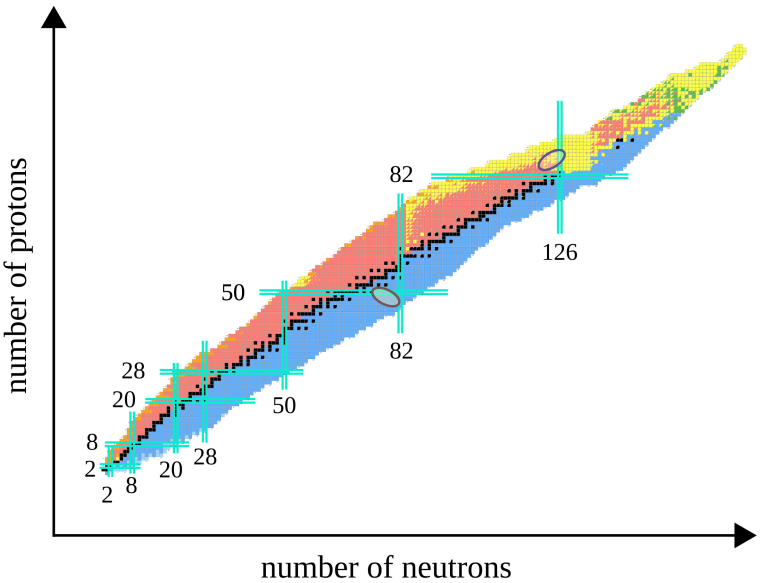


**Figure 1.1:** Nuclear chart of the known isotopes [7], sorted according to their neutron and proton numbers. The colour of each isotope indicates its dominant decay mode: stable (black), $\beta^-$ decay (blue), $\beta^+/EC$ decay (red), proton emission (orange), neutron emission (light blue), $\alpha$ decay (yellow), and spontaneous fission (green). The encircled regions correspond to the $^{213}$Ra decay path (top right) and the nuclei involved in the $\beta$ decay of $^{127}$Cd studied in this thesis. Magic proton and neutron numbers are indicated by cyan lines.

Those models need to be tested and improved by studying those nuclei which are as close as possible to the $r$-process path, but still accessible by accelerator facilities. The $\beta$ decay of $^{127}$Cd to $^{127}$In, which is studied within this thesis, is one such example.

One of the major challenges of investigating nuclei, which are produced artificially in accelerator facilities, is that they are often produced alongside many other nuclei, which then have to be filtered out. Penning traps are state-of-the-art tools to not only select the desired nuclei, but also allow for a distinct selection of a nuclear quantum-state. This unique asset has been utilized to study the decay path of $^{213}$Ra, the $\beta$-decay of $^{127}$Cd/$^{127m}$Cd and the proton decay-branch of $^{53m}$Co. The focus of this work is on the former two experiments. In case of the $^{213}$Ra and $^{53}$Co studies, this exclusive separation enabled revising and measuring nuclear decay properties by confronting the experimental measurements with the results from detailed 'virtual experiments', i.e. Geant4-

simulations [8, 9]. The findings are subject to Papers I, II, and IV. Further details on the study of the decay path of $^{213}$Ra and on the methodology of comparing the simulated experiment with the experimental observation are discussed in chapter 5. The results of the $^{127}$Cd experiment and their interpretation in terms of comprehensive shell-model calculations are presented in Paper III. Detailed aspects of the analysis are provided in chapter 6. The experimental scheme realized in the corresponding experiments is detailed in chapter 2, followed by a discussion on the data calibration and preprocessing in chapter 3. A brief introduction to the theory relevant for the $^{127}$Cd study in particular is given in chapter 4.

# Chapter 2

# Experimental Scheme

To study nuclei that are unstable and therefore do not exist naturally on Earth, they are typically produced artificially in large international accelerator facilities. The data for the heavy nucleus $^{213}$Ra stems from an experiment conducted at GSI Helmholtzzentrum für Schwerionenforschung in Darmstadt, Germany. The experiments I199 and I221 for the somewhat lighter nuclei $^{53}$Co and $^{127}$Cd where conducted at the Ion Guide Isotope Separation On-Line (IGISOL) Accelerator Facility at the University of Jyväskylä, Finland.
The underlying idea to produce unstable nuclei is often similar: an isotopically clean beam of stable nuclei is directed towards a target of isotopically highly enriched material. Upon impact, the beam and target nuclei can undergo a wide variety of reactions, which in turn leads to the production of many different and usually unstable nuclei. In order to explicitly study an isotope which is produced in such a reaction, other reaction products have to be filtered out before the secondary beam of the isotope of interest reaches the detector setup. There the decay of the selected nuclei is investigated.
Depending on the facility and the aim of the experiment, beam, target, and subsequent instruments for filtering the products of the reaction are differently designed.
Figure 2.1 schematically shows the two experimental schemes used for the different experiments which are discussed in the following sections. Further details for the individual setups can be found in the corresponding Papers II, III, and IV.

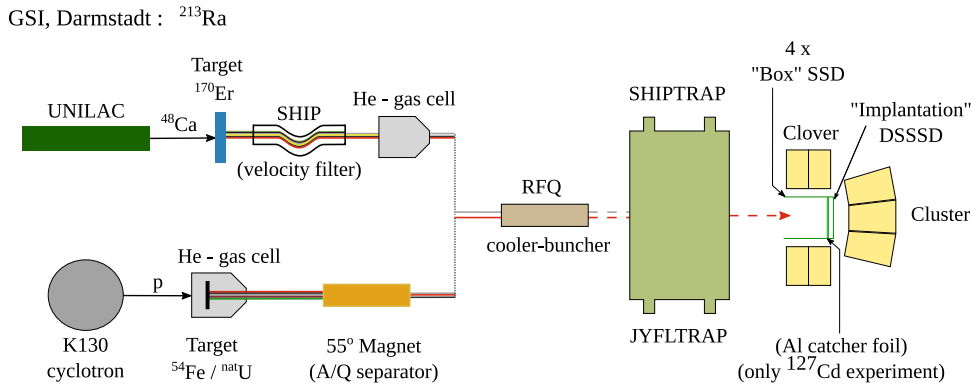


**Figure 2.1:** Sketch of the experimental scheme used for the experiments discussed in this work. The experimental scheme of the $^{213}$Ra experiment conducted at GSI differs slightly from the scheme of the $^{53}$Co and $^{127}$Cd experiments conducted at IGISOL. Conceptually, however, they are the same: the primary $^{48}$Ca (proton) beam for the $^{213}$Ra ($^{53}$Co and $^{127}$Cd) experiment is delivered by UNILAC (K130 cyclotron) and is directed towards the target. There, the nuclear states of interest are formed. The first separation from other reaction products is achieved by SHIP (55° dipole magnet). After the RFQ cooler and buncher the filtered reaction products are transferred to the Penning trap SHIPTRAP (JYFLTRAP). Finally, the ions in the desired nuclear state are selected by the Penning trap and sent into the TASISpec detector setup, consisting of silicon strip detectors (SSD) and HPGe detectors. See text for details.

## 2.1 The $^{213}$Ra Experiment

To produce $^{213}$Ra a beam of $^{48}$Ca ions provided by the UNIversal Linear ACcelerator (UNILAC) [10] was directed towards a rotating target wheel with enriched $^{170}$Er segments (see figure 2.1, upper part). The nuclei of interest were produced via the fusion-evaporation reaction $^{170}$Er($^{48}$Ca, $5n$)$^{213}$Ra, which is depicted in figure 2.2(a). To separate these nuclei from other reaction products and scattered beam particles, the beam was first guided through the Separator for Heavy Ion reaction Products (SHIP) [11]. SHIP is a velocity filter, exploiting the fact that the heavy reaction products from fusion-evaporation reactions are slower than reaction products produced in other reactions or beam particles which did not interact with the target. The filtered beam was then stopped, bunched, and injected into the Penning trap SHIPTRAP [12]. After being mass selected in the trap all ions leaving the trap are to 100 % the desired $^{213}$Ra ions

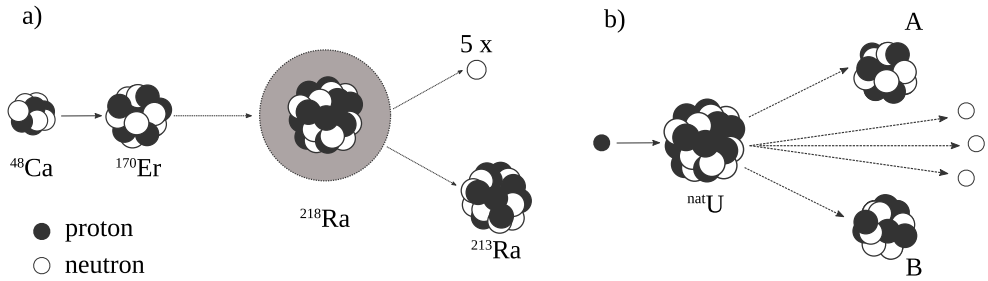


**Figure 2.2:** Depiction of the reaction mechanisms used in the experiments. (a) A fusion-evaporation reaction, using a beam of $^{48}$Ca impinging on a $^{170}$Er target forming an excited $^{218}$Ra nucleus as a compound nucleus. Amongst other reaction products, $^{213}$Ra is produced by evaporating five neutrons. (b) A proton-induced fission reaction used for the production of $^{127}$Cd. A proton beam is directed towards a target of natural Uranium, which fissions into two fission fragments A and B and a varying number of neutrons.

in the nuclear grounds state (see section 2.3). On average, one ion with charge state $2^+$ was extracted per 400 ms cycle, resulting in $\approx$ 2.5 ions per second. Provided the $\approx$ 15 h beam time, the total number of implanted $^{213}$Ra ions can be therefore estimated to $\approx$ 135000. However, the measurements for the number of ions per release before and after the experiment have been conducted with different beam intensities and release frequencies. This and fluctuating beam intensities during the experiment imply a rather large uncertainty on the total number of ions. After the extraction, the ions were post-accelerated to roughly 3 keV and delivered to the decay spectroscopy setup TASISpec (see section 2.4). Such a low kinetic energy of the ions implies that they are rather deposited on the dead-layer of the implantation DSSSD (see figure 2.1), than actually implanted into the active detector volume.

## 2.2 I199 & I221 - $^{53}$Co & $^{127}$Cd

The nuclei or, more precisely, the nuclear states of interest for the $^{53}$Co and $^{127}$Cd experiments were produced by protons delivered from the K130 cyclotron impinging on a $^{54}$Fe or a $^{nat}$U target, respectively (see figure 2.1, lower part). The former reaction produces $^{53}$Co, $^{53m}$Co, $^{52}$Fe and $^{53m}$Fe in knockout reactions, removing protons and/or neutrons from the $^{54}$Fe core. In the latter case, $^{127}$Cd is produced via proton-induced nuclear fission, which is depicted in fig-

ure 2.2(b). All reaction products are immediately stopped in a helium gas cell, extracted and re-accelerated to 30 kV. A first step of separation of the desired nuclei from other reaction products is achieved by a 55° dipole magnet, which has a mass resolution of $m/\Delta m \approx 500$ [13]. This is sufficient to filter all nuclei with the required mass number $A$. Thereafter, similar to the $^{213}$Ra case and as indicated in figure 2.1, the remaining ions are cooled, bunched, and injected into the Penning trap JYFLTRAP. The IGISOL facility and JYFLTRAP are described in detail in references [14] and [15]. After being separated by JYFLTRAP, only the ions of interest, in their ground state and/or isomeric state, are transferred to the TASISpec decay spectroscopy setup (see section 2.4).

## 2.3 Penning Trap Assisted Decay Spectroscopy

Penning traps are the most precise tools available today to measure nuclear masses, reaching precisions of up to $m/\Delta m \approx 10^9$ in dedicated mass measurements (e.g. [16, 17]). Even for a heavy nucleus like $^{213}$Ra this would correspond to less than 1 keV mass resolution. In comparison, the common distance between nuclear states reaches from a few keV up to several MeV. The technique itself, however, is limited to nuclei which have half-lives on the order of about 100 ms or longer. At the same time short half-lives compromise the achievable mass resolution. Hence, Penning traps are able to separate on the level of individual nuclear states, provided they have long enough half-lives. Placing a detector setup like TASISpec (see next section 2.4) behind a Penning trap allows one to study the decay sequence of mass selected nuclei or decays of specific nuclear states. Depending on the necessary mass resolving power the trap must achieve for an experiment, different techniques can be used. A mass-selective buffer gas cooling technique [18] is sufficient for resolving powers on the order of $10^5$, which are needed for the $^{213}$Ra experiment and the $^{53}$Co experiment. In case that resolving powers larger than $10^6$ are needed, methods like the Ramsey cleaning method [19] or the phase-dependent cleaning method [16, 17] in conjunction with the buffer gas cooling technique have to be employed. Obviously, better resolving powers require additional manipulation of the ions inside the Penning trap, often leading to longer cycle times. Hence, a higher resolving power always implies a lower rate of ions delivered to the decay spectroscopy setup, and therefore less statistics during the experiment.

### 2.3.1 $^{213}$Ra

In case of the $^{213}$Ra experiment already a resolving power of $m/\Delta m \approx 72000$, corresponding to 2.7 MeV and a cycle time of 400 ms was sufficient to prepare a beam consisting of only $^{213}Ra^{2+}$ ions in its ground state: The 5.7 MeV heavier $^{213}$Ac cannot be produced with the used beam-target combination. $^{213}$Fr is only 3.9 MeV lighter than the $^{213}$Ra ground-state and can therefore not be clearly separated by the Penning trap only. However, because its second ionization potential is similar to the first ionization potential of Helium, which is used in the stopping cell, no doubly charged $^{213}$Fr ions reach the trap [20]. Finally, the 1770 keV isomer in $^{213}$Ra has a half-life of only 2.15 ms and decays before the beam is delivered to TASISpec. Hence, it is solely the $^{213}$Ra ground state that is leaving the trap.

### 2.3.2 $^{53}$Co

For the $^{53}$Co experiment at Jyväskylä the $^{53}$Co ground-state and its roughly 3.2 MeV heavier isomeric state had to be studied individually. These states can be well separated with a resolving power of $m/\Delta m \approx 50000$ corresponding to 1 MeV. As the neighbouring nuclei $^{53gs}$Fe and $^{53m}$Fe are 8.3 MeV and 5.2 MeV lighter, respectively, they are easily separated as well.

### 2.3.3 $^{127}$Cd

To separate the 300-keV $^{127}$Cd isomer from the $^{127}$Cd ground state, a much higher resolving power is needed. At first a feasibility study was conducted, using $^{125}$Cd, which is produced with a higher yield than $^{127}$Cd. Using only the buffer gas cooling technique and a trap cycle time of 140 ms, the $^{125}$Cd ground state together with its $\approx 190$ keV isomer could be separated from other $A = 125$ isobars. Achieving a rate of some 100 ions per second delivered to TASISpec, the observation of expected $\gamma$-ray transitions in $^{125}$In [21] quickly identified and verified the incoming ions to be $^{125}$Cd. Employing the Ramsey cleaning method, the $^{125}$Cd isomer could be selected and $\approx 10$ ions per second were delivered to TASISpec. Again, the expected $\gamma$-ray transitions in $^{125}$In after the $^{125m}$Cd $\beta$-decay could be observed. This was not possible for the $^{125}$Cd ground state, which is produced with less yield than the isomeric state. After $\approx 4.5$ h of measuring the $^{125}$Cd ground-state $\beta$-decay, no $\gamma$-ray transitions correlated to that decay could be observed.

As it was the case for $^{125}$Cd, the ground state together with the isomeric state of $^{127}$Cd could be separated from other $A = 127$ isobars by employing the buffer gas cooling technique, delivering $\approx 10$ ions per second. The rate was primarily limited by the amount of $A = 127$ isobars in the incoming beam, which were saturating the Penning trap. This problem became even more pronounced when attempting to select $^{127m}$Cd with the Ramsey cleaning method. Another attempt was made by employing the phase-dependent cleaning method. The results of a $\approx 11$ h long run of $^{127m}$Cd are presented in section 6.3. Due to the very low rate of 20 ions per minute, no further cleaning beyond the buffer gas cooling technique was used for the remaining beam time.

### 2.3.4 Trap Release Cycle Considerations

Since one aim of the $^{127}$Cd experiment was to determine the half-life of $^{127}$Cd, an estimate for an optimal trap release cycle had to be made beforehand. To a first order approximation there are two competing aspects: on the one hand, the shorter the trap release cycle, the less prominent are the features of the exponential decay curve (see equation 2.1), since the reference time, which is the trap release signal, for a detected decay is reset with each trap release. On the other hand, a longer trap release cycle implies that less ions are delivered per unit time. Hence fewer ions are delivered during a fixed experimental time, imposing on the statistics available for, e.g., studies of $\gamma$-ray transition intensities.

$$I(t) = I_{t=0}\, e^{-\lambda t} \tag{2.1a}$$

$$T_{1/2} = \frac{ln2}{\lambda} \tag{2.1b}$$

Based on the expected numbers of $^{127}$Cd ions in the proposal and the hitherto reported half-life of $T_{1/2} = 370(70)$ ms [22], an exponential decay curve has been sampled and cut into time intervals corresponding to the anticipated trap cycle. By adding up the statistics of these intervals, one mimics the reset of the reference time for a detected decay with each trap release signal. The obtained spectrum is then approximated with an exponential function, resulting in an estimate for the underlying half-life. Repeating this several times with different seeds for the random number generator, one obtains a Gaussian distribution of this estimate and can deduce its expected uncertainty. This has been done for a number of different trap release cycles.
The amount of sampled decays has been adjusted corresponding to the trap release cycle, i.e. a twice as long trap release cycle implies just half as many

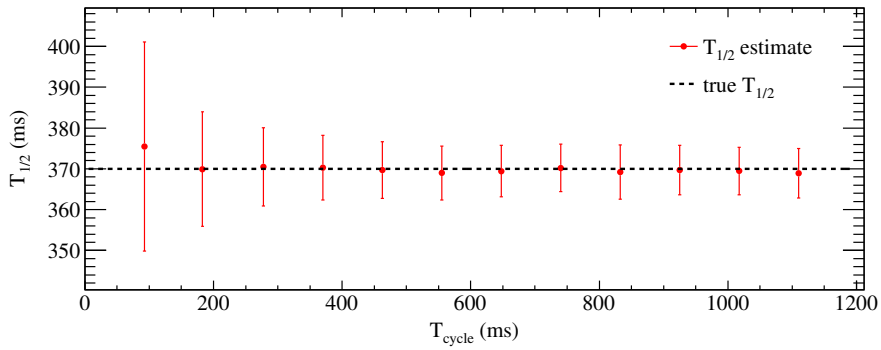


**Figure 2.3:** The estimated half-life of an exponential decay with $T_{1/2} = 370\,\text{ms}$ for varying trap release cycles, $T_{cycle}$. For longer trap release cycles the estimate suffers from less statistics, because fewer ions are released per unit time. Therefore, the uncertainty of the estimate does not improve further. For trap release cycles longer than some two half-lives of the investigated nucleus, the uncertainty starts to increase again.

released ions. The result is shown in figure 2.3. One can see that a trap release cycle longer than one half-life of the investigated nuclear state does not significantly improve the estimates of the half-life. Already with a trap release cycle of about $T_{cycle} \approx \frac{1}{2}T_{1/2} = 185\,\text{ms}$ one can improve the estimate of the half-life compared to the reported half-life. A longer trap release cycle would lead to a slightly improved half-life estimate. However, it would also imply that fewer ions are delivered to the detector setup which results in less statistics available for the $\gamma$-ray spectroscopy study of $^{127}$In, the $\beta$-decay daughter of $^{127}$Cd.

## 2.4 TASISpec

Figure 2.5 shows the decay-spectroscopy setup TASISpec [23] as it was used in the $^{127}$Cd experiment (compare with figure 2.1). Its core is formed by a cube of five $6 \times 6\,\text{cm}^2$ Silicon Strip Detectors (SSD) for charged particle detection, which can be seen in figure 2.4. Those ions that have been selected by the Penning trap are sent into the cube and onto a Double Sided Silicon Strip Detector (DSSSD), called *'implantation'* DSSSD. Because of their comparably low kinetic energy (3 keV in case of $^{213}$Ra and 30 keV in case of the $^{53}$Co and $^{127}$Cd experiments), the ions are stopped within the $\approx 2\,\mu$m thick $SiO_2$ dead-layer of the implantation DSSSD. This particularly affects the detection of protons and $\alpha$ particles, which is discussed in section 5.2. Another implication is that no implantation signal is available.

To detect $X$ rays and $\gamma$ radiation, the SSD cube is surrounded by High Purity Germanium (HPGe) detectors. A Cluster detector comprising seven individual HPGe crystals [24, 25] was positioned behind the implantation DSSSD. Depending on the experiment, one up to three clover detectors comprising four individual HPGe crystals [24–27] were positioned behind the other four *'box'* SSDs.
For the $^{127}$Cd experiment an Anti Compton Shield (ACS) was available for the GREAT clover [27] positioned below the silicon cube (see figure 2.5). An attempt was made to lower the Compton background for the other HPGe detectors as well by attaching several small Bismuth Germanate (BGO) anti Compton detectors around the cluster detector and the two other clover detectors. In the same experiment, a 9 $\mu$m thin aluminium foil was placed in front of the implantation DSSSD, so that the ions from the Penning trap were already implanted there instead of the implantation DSSSD (see figure 2.4). Consequently, long-lived daughter activity, and therefore background radiation, could be removed by simply exchanging this foil. This was especially necessary after the feasibility study with $^{125}$Cd to remove activity from $^{125gs}$Sn, which has a half-life of 9.6 days [21].
In the $^{53}$Co and $^{127}$Cd experiments, the signals of the silicon detectors (as well as the ACSs in the $^{127}$Cd experiment) were read out and digitized by FEBEX modules [28] with 14-bit sampling at a rate of 50 MHz. The further processing of the digitized signals is described in section 3.1. In section 3.2 the treatment of the HPGe detector signals is discussed.

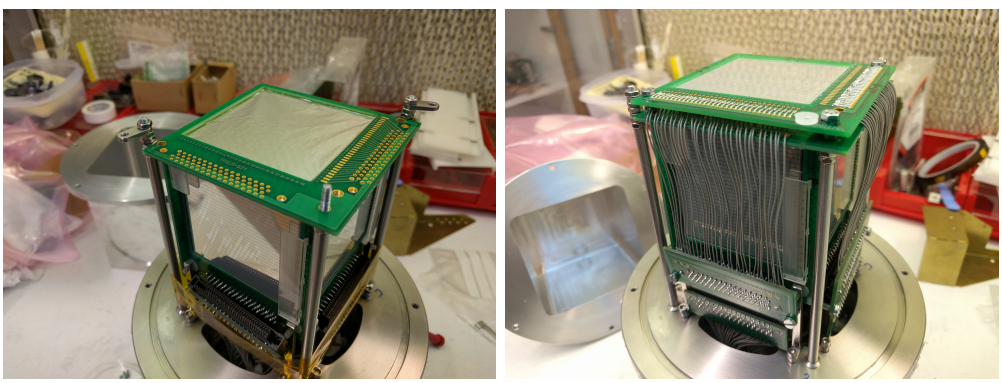

**Figure 2.4:** The TASISpec cube of five silicon detectors for charged particle detection in preparation for the $^{127}$Cd experiment. (Left) The implantation DSSSD is removed and an aluminium catcher foil is installed. (Right) The implantation DSSSD is placed 6 mm behind the aluminium catcher foil.

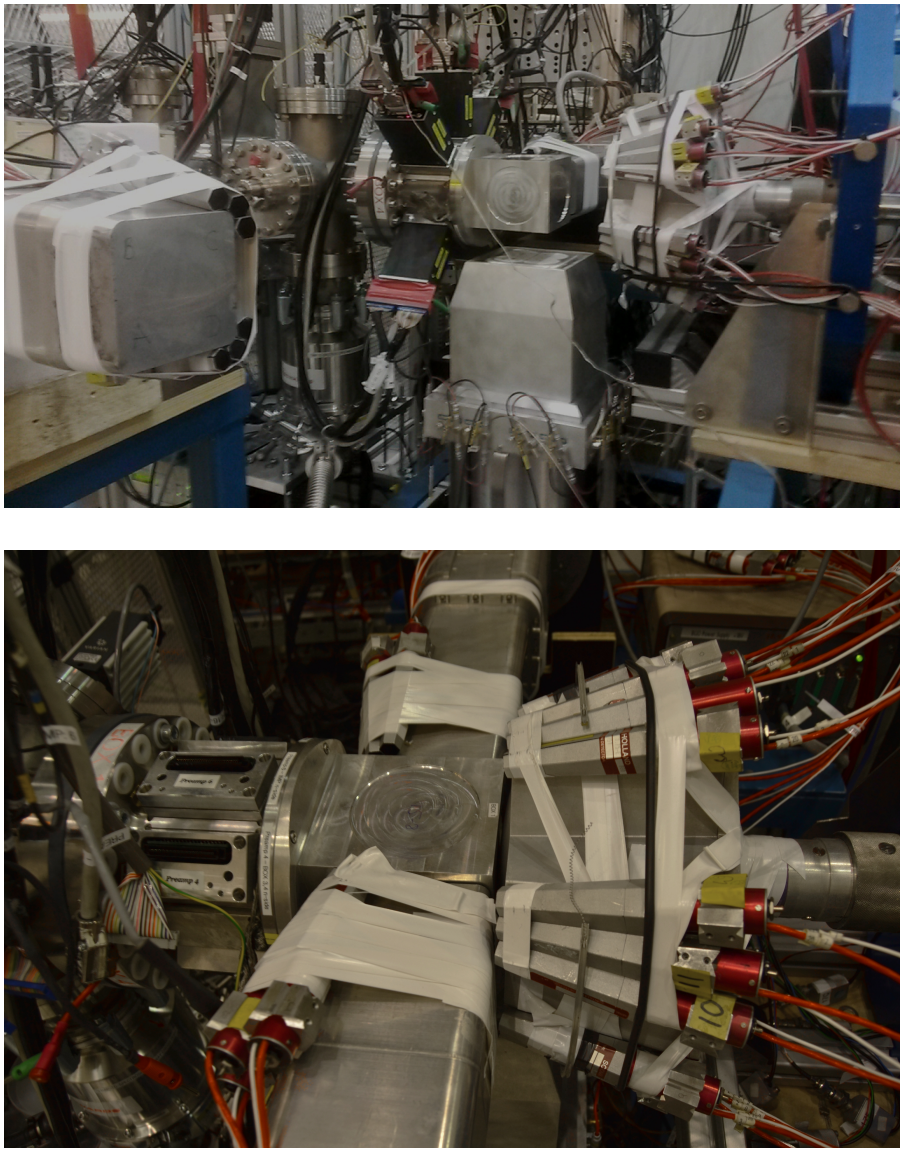

**Figure 2.5:** The TASISpec setup at the $^{127}$Cd experiment with one clover and the cluster pushed back (top) and with the HPGe detectors in nominal position (bottom). The $^{127}$Cd ions selected by JYFLTRAP are incoming from the left.

# Chapter 3

# Data Calibration and Preprocessing

Before analysing the recorded data from a physics perspective, the data has to be calibrated and preprocessed to improve the quality of the data set. Using the experimental data from the $^{127}$Cd experiment, the following sections discuss the most important aspects. The procedure and techniques are similar in case of the $^{213}$Ra experiment. However, there the data calibration and preprocessing was readily done using tscan, a list-mode analysis framework written in the programming language C.
The binary data files from the $^{127}$Cd experiment were first read with the GO4 analysis framework [29], where primarily the traces of the silicon detectors were analysed (see section 3.1), the data presorted, compressed and stored in ROOT TTrees [30, 31]. Thereby the information of a raw data file from the MBS data acquisition system [32] could be compressed from $\sim 1\,\mathrm{GB}$ to $\sim 2\,\mathrm{MB}$ ROOT files containing a TTree with about 25000 events. These data objects are much faster to read and process in the further analysis. Each entry in the TTree contains the following information of one event: (uncalibrated) energy, time, and detector number of each signal detected in that event as well as trigger information and the time of the internal clocks of the FEBEX and SIS modules. Based on these TTrees, further processing, including the option of so-called add-back procedures, energy and time calibration of all detectors was performed using the ROOT framework [30, 31] and the programming language C++.

## 3.1 Processing of DSSSD and ACS data

### 3.1.1 DSSSD traces

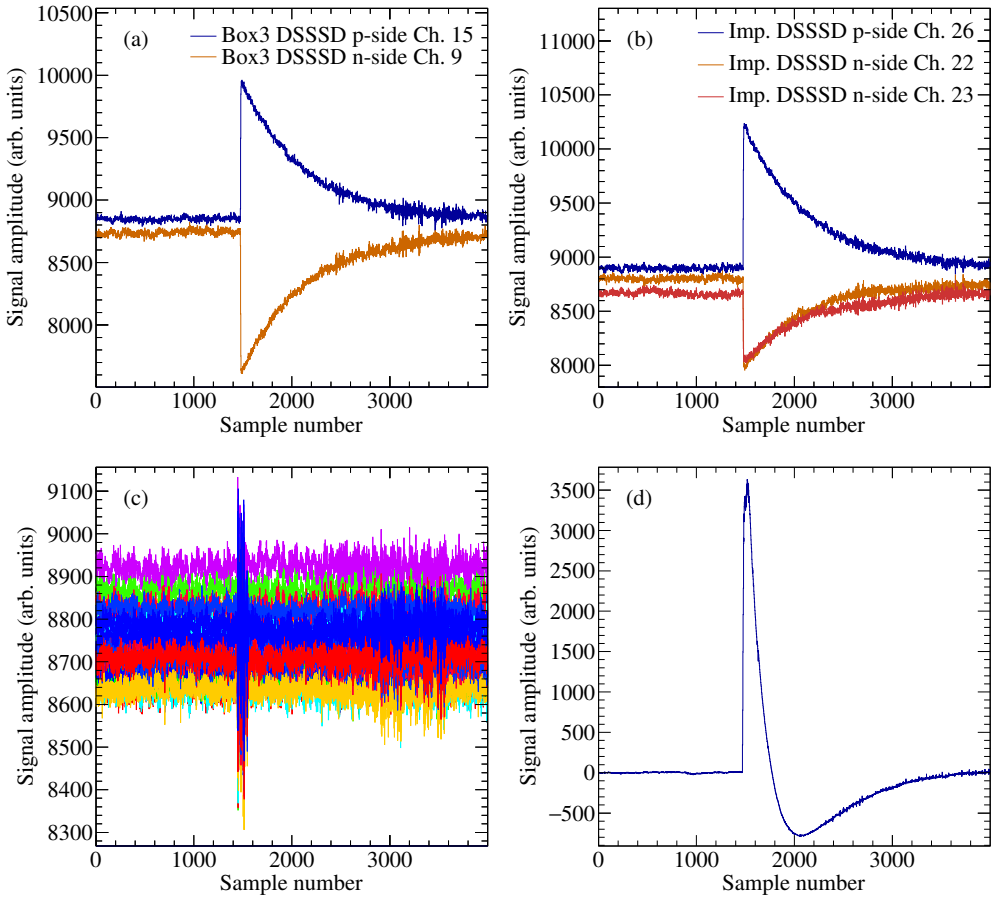


**Figure 3.1:** Digitized signals, *traces*, from the DSSSDs. (a) A normal charged particle event where a p-side and a n-side strip of the same DSSSD have signals corresponding to the same deposited energy. (b) Same as (a) but here the particle hit in between two neighbouring n-side strips. (c) An event where 41 out of the 64 strips of the implantation DSSSD reacted to electrical noise. (d) A baseline corrected trace recorded from GREAT Anti Compton Shield (ACS). See text for details.

The digitized signals from the DSSSD detector preamplifiers, called *traces*, have a length of 4000 samples, where each sample corresponds to $\frac{1}{50\,\mathrm{MHz}} = 20\,\mathrm{ns}$. Two examples from a p-side and n-side of a DSSSD detecting a $\beta$ particle can be seen

in figures 3.1(a) and (b). The signal height with respect to the baseline of the signal corresponds to the collected charge in the detector and is to good approximation proportional to the energy deposited in the detector. The baseline value is calculated as an average of the first 1500 samples of each individual trace. To extract energy and time information from the recorded traces, a short trapezoidal filter in combination with a Moving Window Deconvolution (MWD) was applied (see, e.g., references [33] and [34]). In short, the trapezoidal filter 'detects' the signal in a trace and extracts its position, i.e. its time. In turn, the MWD is used to extract the energy information of such a trace. One important parameter in the MWD is the decay time, $\tau$, of the signal, which primarily depends on the preamplifier of each DSSSD channel. Hence, the decay time has been determined for each single strip for each DSSSD individually by summing up several hundred traces for each strip and approximating the resulting sum with an exponential function. The determined decay times are on average $\sim 13\,\mu$s. By tuning the parameters of the short trapezoidal filter, it was possible to identify traces which were actually just electrical noise, but large enough to trigger the data acquisition system. An example of such an event is shown in figure 3.1(c), where nearly all channels from the implantation DSSSD triggered the data acquisition system. It turns out that this was the case for about 80% of all the recorded traces in the $^{127}$Cd experiment. On the one hand, it could indicate too low threshold values in the MBS data acquisition system during data taking. On the other hand it appears that this is mainly a problem of the implantation DSSSD, where about 90% of all the recorded traces are noise triggered.

As can be seen in figure 3.6, roughly at 1 ms and 11 ms after a trap release the recorded event rate drops suddenly and recovers again after about 3 ms. Just before the sudden drop, the event rate is more than two times higher than the average event rate. This seems to be correlated to the closing of the trap 1 ms after the trap release, which seems to induce strong noise primarily in the implantation DSSSD and therefore in most of its 64 strips. Thereafter, the data acquisition is busy processing, buffering and writing the corresponding traces, so that it cannot take any new trigger requests for some time. This could explain the overall high amount of recorded noise.

The filtering of those noise-triggered traces and the extraction of time and energy information from the good traces are the main factors for the compression of the MBS files to ROOT files.

### 3.1.2 ACS traces

Traces from the GREAT-clover ACS look very different than traces from the silicon detectors, as can be seen in figure 3.1(d). Hence, a MWD cannot be applied. However, the energy information of these signals is not of relevance for the analysis. The information *if* and *when* there has been a signal in the ACS is sufficient to identify a detected signal in an adjacent GREAT-clover HPGe crystal as a possible Compton-scattered photon. Since the signals have a large amplitude it is adequate to simply store a boolean veto flag and the corresponding time in the TTree if the signal of an ACS trace reaches a threshold amplitude of 500. After a time calibration as it was done for DSSSDs, a time resolution of the ACS shield of 170 ns was obtained. This value is well within the energy-time gate condition applied on the detected photons (see section 3.2).

### 3.1.3 Further treatment of DSSSD data

As a next step each individual strip of each silicon detector was energy calibrated using standard radioactive sources. In case of the $^{127}$Cd experiment it was done using a $^{207}$Bi source. Similarly the event time for each strip has been calibrated so that all strips have the same time with respect to the event trigger time stamp. To reduce random background or noise which could not be filtered out during the processing of the traces, only those silicon signals are used which are prompt with respect to the trigger signal. This is illustrated in figure 3.2(a). If a charged particle hits a silicon detector, a positive signal is induced in a p-side strip and a negative signal with the same amplitude in a n-side strip, as shown in figure 3.1(a). Hence, an event was rejected if no such pair of p-side strip and n-side strip with the same energy (within a margin of $\pm 1\,\%$) could be found. In some cases a charged particle does hit the region between two strips, so that the two strips share the induced charge. An example of such an event can be seen in figure 3.1(b). Consequently, such an event would be rejected because there is no matching pair of p-side and n-side signal. In order to take these *inter-strip* events into account, nearest neighbour add-back is performed: if two neighbouring strips are hit, their energies are *added back* and the resulting sum energy is assigned to the strip which had the higher signal amplitude.
In the further analysis, see chapter 6, only events fulfilling these requirements are considered. These constitute around 70 % of all the particle-triggered events, after exclusion of noisy traces.

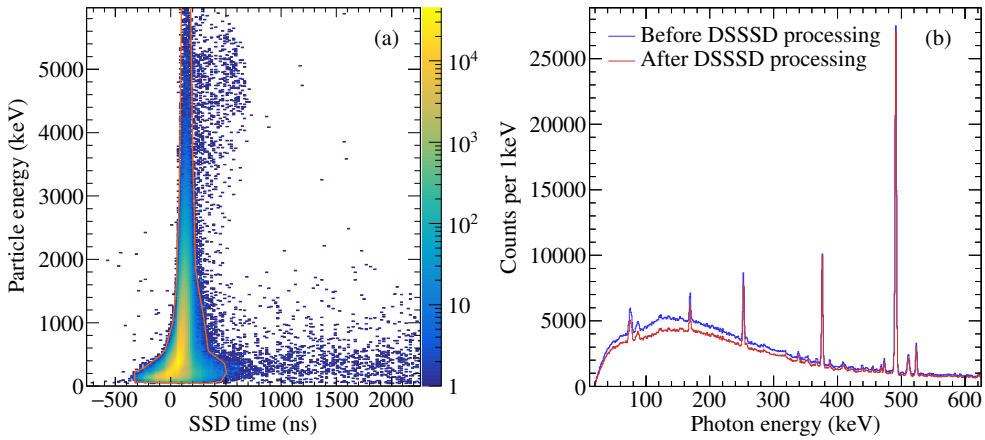


**Figure 3.2:** (a) Correlation between the energy and time of charged particles detected with the DSSSDs during the $^{127}$Cd experiment as well as the gate condition to reduce random background. (b) Resulting improvement on the photon spectrum in prompt coincidence with a charged particle after applying the gate condition seen in panel (a), inter-strip add-back and requiring matching pairs of p-side and n-side signals.

## 3.2 Processing of HPGe detector data

The signals from the HPGe detectors are processed by commercial SIS3302 sampling ADCs. The HPGe signals are digitized and energy as well as timing information of a signal are extracted by the firmware and included in the MBS data stream. Hence, detailed processing of traces, as it was necessary/possible for the silicon detector signals, does not apply for the SIS3302 setting used in this experiment.

### 3.2.1 Baseline correction

Alongside energy and time, the value of the baseline is recorded, too. The importance of the baseline information is illustrated in figure 3.3. Panel (a) shows a two dimensional plot of the baseline value vs. the uncalibrated energy. One can see that the delivered energy value from the ADC depends on the baseline value. At higher event rates (on the order of several kHz) it can happen that a photon is detected in a HPGe detector before the signal of a previous detection has reached the standard baseline value again (so-called 'pile up'). Therefore, the baseline value for the later signal is estimated too high, and the computed

energy value is too low. This leads to clearly visible tails at the low energy side of the recorded $\gamma$-ray peaks, which are obvious in figure 3.3(b). Since the baseline-energy correlation appears to be linear to a very good approximation, this effect can be easily corrected for. The result is shown figures 3.3(c) and (d). Here, the baseline correction as well as the energy calibration has been applied. The peaks have no tails any more, which leads to a significantly improved energy resolution. This correction was determined and applied for each HPGe crystal individually.

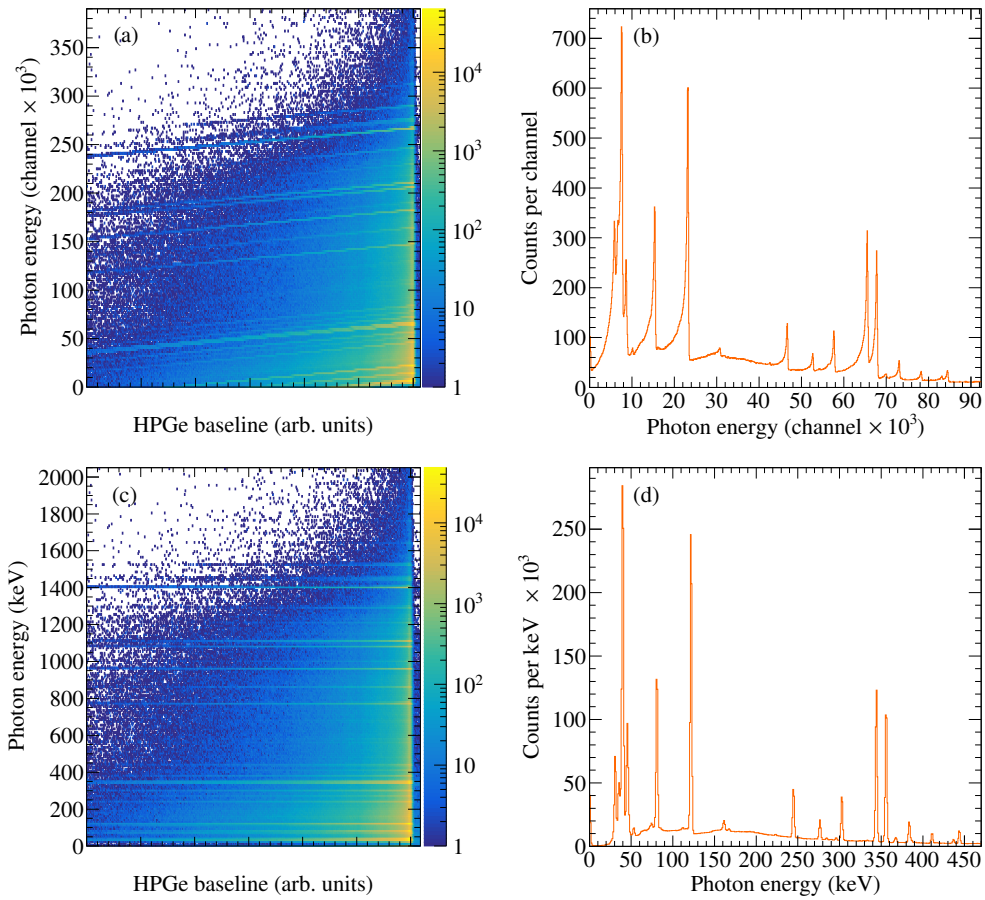


**Figure 3.3:** (a) Correlation between the uncalibrated photon energy and the baseline value provided by the SIS3302 sampling ADC for the central HPGe crystal of the cluster detector. (b) Energy projection of (a). (c) and (d) are the corresponding figures after baseline correction and energy calibration. The data stems from a calibration measurement after the $^{127}$Cd experiment with an intense mixed $^{152}$Eu-$^{133}$Ba source.

### 3.2.2 Energy calibration

The energy calibration of the HPGe detectors was done using a mixed $^{152}$Eu-$^{133}$Ba source, which provides calibration energies from 40 keV up to 1.5 MeV. In addition to these, intense background $\gamma$ radiation from $^{40}$K, $^{214}$Bi, and $^{208}$Tl decays could be used to obtain calibration energies at 1460.8 keV, 1764.5 keV, and 2614.5 keV, respectively. The calibration was obtained using equation 3.1. Below an energy of 1408 keV a calibration with a second order polynomial with an additional square-root term was used. Above this energy a linear calibration was found to provide the most reliable energy calibration. The 1408 keV transition is the most intense $\gamma$-ray transition from the $^{152}$Eu decay above 1 MeV and was included in both parts of the calibration curve. In this way a smooth transition between the low-energy and the high-energy part of the calibration is ensured.

$$E_{cal}(E_{CH}) = \begin{cases} \sum_{i=0}^{2}(a_i E_{CH}^i) + a_3\sqrt{E_{CH}} & \text{for } E_{cal} \leq 1408\,\text{keV} \\ \sum_{i=0}^{1}(b_i E_{CH}^i) & \text{for } E_{cal} \geq 1408\,\text{keV} \end{cases} \tag{3.1}$$

The uncertainty of the calibration of energies up to 1.4 MeV is 0.1 keV to 0.2 keV. For higher energies up to the last calibration point at 2.6 MeV, the energy calibration has an uncertainty of up to 0.4 keV.
To correct for possible gain shifts of the HPGe detectors over time, a linear recalibration was done for every $\sim 7$ h of measurement time. Well known energies of daughter decays and background radiation were used.
Similar to the silicon detectors, each HPGe crystal was time aligned such that it is prompt with respect to the event trigger.

### 3.2.3 Background reduction

As it was done for the data from the silicon detectors, a prompt energy-time gate condition was applied to suppress random background, which is indicated in figure 3.4(a). Its width ranges from $\approx 750$ ns for energies at around 50 keV to $\approx 250$ ns for energies above 1500 keV. The same energy-time gate but shifted by 2 $\mu$s was used to define a background gate. Events that are within the background gate are clearly uncorrelated to the trigger at time $t = 0$. Subtracting those events from the photon events in the prompt gate removes therefore the random background in the prompt gate. The effect is nicely visible for instance in figure 3.4(b), where the 1461-keV $\gamma$-ray peak from the $^{40}$K decay disappears after the prompt energy-time gate is applied *and* the background subtracted.

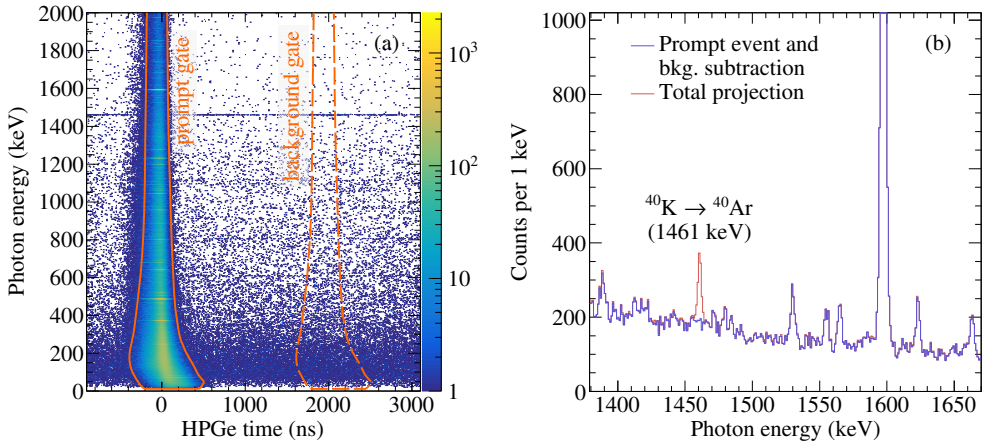


**Figure 3.4:** (a) Correlation between the energy and time of photons detected with the HPGe detectors during the $^{127}$Cd experiment in prompt coincidence with a particle detected in a silicon detector as well as the gate conditions for prompt and random background events. (b) Portion of the total projection of panel (a) together with the spectrum after applying the prompt gate condition and subtracting the background obtained from the background gate condition.

Another possibility for background reduction is provided by the GREAT-clover ACS (see section 3.1.2): if a detected photon in a GREAT-clover HPGe crystal is in prompt coincidence with a signal from an adjacent ACS crystal, i.e. both signals are within the energy-time gate shown in 3.4(a), the photon is rejected.

### 3.2.4 Add-back

The last step to improve the quality of the photon spectrum is add-back. If two signals in two HPGe crystals are detected in prompt coincidence, then they might not stem from two independent photons, but from a single photon which first Compton scattered in one crystal and deposited its remaining energy in another crystal. Hence, by adding back energies detected in prompt coincidence in two crystals which are spatially close, the energy of the initial photon can be reconstructed and the Compton background reduced.
Figure 3.5 shows how different add-back conditions affect the resulting photon spectrum. The total spectrum comprises events with both trigger types: particle trigger and photon-photon coincidence trigger. As a first level of add-back only the nearest neighbouring (NN) crystals which are part of the same detector are considered for add-back. Clearly the Compton background at low energies is

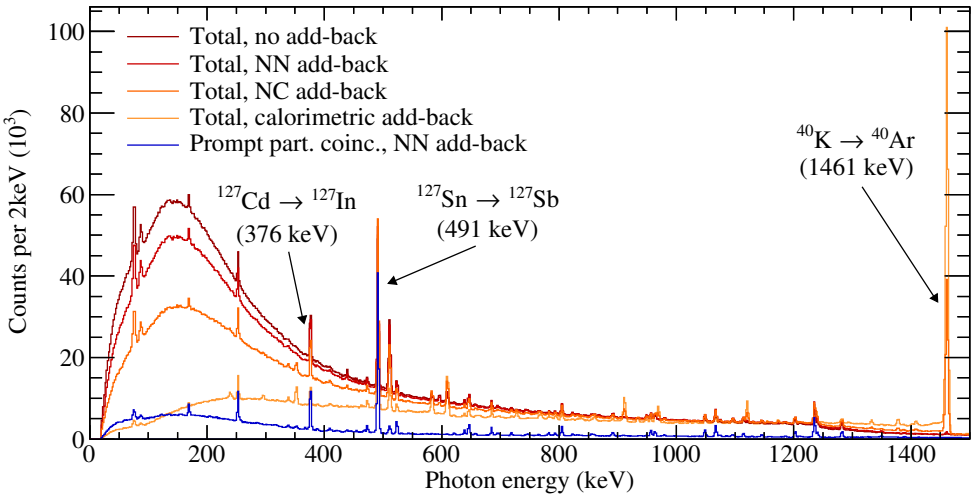


**Figure 3.5:** Effect of different add-back methods (NN: nearest neighbor; NC: neighboring crystal) on the photon spectrum of the $^{127}$Cd experiment. The total spectrum includes events triggered by a charged particle detection and photon-photon coincidence triggered events.

reduced significantly. The next add-back level shown in figure 3.5 also adds back photon energies if they were detected in neighbouring crystals (NC) from different detectors. Finally, one can also add back all photon energies detected within one event (calorimetric add-back). For the latter two add-back levels, the 'sudden' appearance of the 1461-keV $\gamma$-ray peak from the $^{40}$K decay is striking. Similarly, other background transitions appear as soon one goes beyond NN add-back, for instance the 2615-keV $\gamma$-ray peak from the $^{208}$Tl decay.
In comparison to the total spectrum also the spectrum with only particle triggered events and NN add-back is shown in figure 3.5. By comparing the total and particle triggered spectrum it is apparent that the relevant information concerning the decay of $^{127}$Cd and the following daughter decays is fully contained in the particle-triggered data. In contrast, the photon-photon coincidence data contains primarily event information from Compton-scattered background radiation. Therefore, the data analysis discussed in chapter 6 was conducted using only events which are in prompt coincidence with a particle.

### 3.2.5 Efficiency

The relative photon detection efficiency of the whole TASISpec setup was estimated using the Radware-EFFIT tool [35]. The function 3.2 is used to approximate the relative efficiency, $\epsilon_{rel}(E_\gamma)$, as function of the photon energy, $E_\gamma$, in keV:

$$\begin{aligned} ln\ \epsilon_{rel}(E_\gamma) &= \{(A + Bx + Cx^2)^{-G} + (D + Ey + Fy^2)^{-G}\}^{-1/G} \\ x &= \ln(E_\gamma/100) \\ y &= \ln(E_\gamma/1000) \end{aligned} \tag{3.2}$$

Using the calibration measurement with the mixed $^{152}$Eu-$^{133}$Ba source and without applying add-back the obtained parameter values for $A$ through $G$ are 6.75(8), 2.75(8), 0(fixed), 3.908(7), −0.806(12), −0.104(6), and 8.9(1), respectively. After NN add-back was performed the parameter values are 10.9(8), 6.1(7), 0(fixed), 4.093(1), −0.675(16), 0(fixed), and 2.2(2)(fixed), respectively. Comparing the resulting efficiencies before and after applying NN add-back, the efficiency improves by about 7 % at 0.5 MeV up to 46 % at 2.5 MeV $\gamma$-ray energy.

## 3.3 Processing of the trap release signal

Every time a bunch of $^{127}$Cd ions was released from the trap and sent towards the TASISpec setup, a trap release signal was sent and triggered the data acquisition system. Therefore, it is possible to relate a detected particle or photon to the last trap release, which is explained further in chapter 6. Sometimes, however, the release signal was missed because the data acquisition system was busy, for instance, processing an event detected shortly before. In figure 3.6 the time of particle triggered events after the last trap release signal is shown. Since the trap cycle was 143 ms long, there should be no event with $t_{event} - t_{trap\ release} > 143$ ms if all trap release signals were recorded. As one can see a number of events (around $\sim 3$ %) missed the last trap release signal, and the pattern between time 0 and 143 ms repeats after 143 ms (the blue spectrum in figure 3.6). Considering that the timing of the trap release signal itself was very reliable and precise (around 10 ns), the trap release signal was artificially included, i.e. *recovered*, in the data stream during the offline analysis if for an event $t_{event} - t_{trap\ release}$ exceeded the trap release frequency by more than 1 $\mu$s.

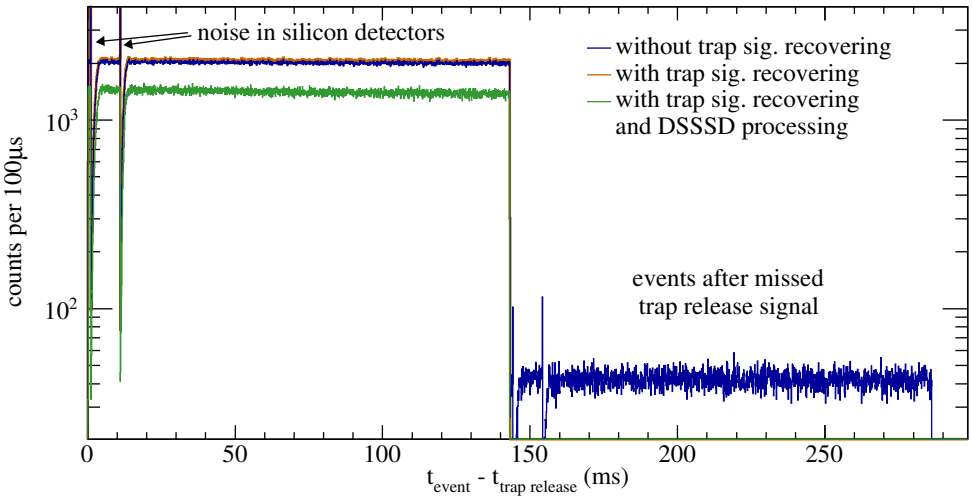


**Figure 3.6:** Time difference between the time of particle-triggered events after the last trap release signal after having processed the DSSSD traces (blue), after including missed trap released signals (orange), and after performing DSSSD add-back and requiring matching hits in n-side and p-side strips, see section 3.1 (green). The orange and blue spectra appear nearly identical between time 0 and 143 ms, see text for details. The features at 1 ms and 11 ms are discussed in section 3.1.

# Chapter 4

# Theoretical Background

This chapter introduces the theoretical background that is necessary to understand and interpret the observed experimental data. Sections 4.1 and 4.2 provide an overview of the nuclear shell model and the NuShellX@MSU code. The latter is used to predict energies and wave functions of excited states as well as transition rates of $\gamma$-ray transitions and allowed $\beta$ decays. In sections 4.3 and 4.4 short introductions to electromagnetic transitions in nuclei as well as $\beta$ decays are given. More detailed and complete theoretical descriptions can be found in, for instance, [2, 36, 37] (shell model, electromagnetic transitions) and [3, 38] ($\beta$ decays).

## 4.1 The nuclear shell model

Studying the properties of nuclei reveals that nuclei with certain numbers of protons, $Z$, and neutrons, $N$, show a significantly enhanced stability against nuclear decay. This implies, for instance, longer lifetimes, high natural abundances, and relatively high proton and neutron separation energies. For nuclei close to the valley of stability (see figure 1.1) these features are found for nuclei with $N$ or $Z$ being one of the so-called *magic numbers*: 2, 8, 20, 28, 50, 82, as well as $N = 126$. This was first recognized by M. Goeppert Mayer [39]. Some nuclei are doubly magic, i.e. have a magic number of protons *and* neutrons. These are, for example, $^{4}$He, $^{16}$O, $^{48}$Ca, $^{132}$Sn and $^{208}$Pb. Having experimentally observed such an apparent *shell* structure, it seems natural to have a theory that inherently reflects this structure.

As with any many-body quantum-mechanical system, the starting point to theoretically describe the atomic nucleus is the Schrödinger equation 4.1.

$$H\psi = E\psi \tag{4.1}$$

The Hamiltonian $H$ consists of a term describing the kinetic energy of the involved nucleons (the first term in equation 4.3 (a)) and a potential describing the interaction between the nucleons. But already a full description of the interaction between all the nucleons in an atomic nucleus proves to be a very difficult task. On the one hand, nucleons interact with other nearby nucleons via the short-range and attractive strong force, which binds them together. On the other hand, the closely packed protons are positively charged and experience a repulsive force due to the long-range Coulomb interaction with all the other protons in the nucleus. A possible approximation is to describe the motion of a nucleon in a common average potential formed by all the other nucleons in the nucleus. Commonly, the Woods-Saxon potential $V_{WS}$ [40] as in equation 4.2 is used, where $V_0$ is the depth and $R$ the radius of the potential, and $a$ the *skin diffuseness* parameter. Then the Hamiltonian for a system of $A$ nucleons with mass $m$ takes the form of equation 4.3. $H_{res}$ describes the residual interaction that is not properly described by the average potential $V_{WS}$.

$$V_{WS}(r) = \frac{-V_0}{1 + \mathrm{e}^{\frac{r-R}{a}}} \tag{4.2}$$

$$H = \sum_{i=1}^{A}(-\frac{\hbar^2}{2m}\nabla_i^2) + \sum_{i=1}^{A} V_{WS}(r_i) + H_{res} \tag{4.3}$$

Solving the Schrödinger equation 4.1 with this Hamiltonian 4.3 results in the eigenstates $\psi_i$ with the energies $E_i$ of the nuclear system. The calculated eigenstates correspond to the single-particle wave functions and can be characterized by a unique set of *quantum numbers*:

- $n = 1, 2, 3, \ldots$ : number of nodes of the radial wave function
- $\ell = 0, 1, 2, \ldots$ : orbital angular momentum quantum number, usually denoted $s$, $p$, $d$, $f$, $g$, $h$, $i$ instead of the integer values 0, 1, 2, 3, 4, 5, 6
- $j = \ell \pm \frac{1}{2}$ : total angular momentum quantum number
- $m_j = -j, -j+\frac{1}{2}, \ldots, j+\frac{1}{2}, j$ : projection of the total angular momentum quantum number on the quantization axis.

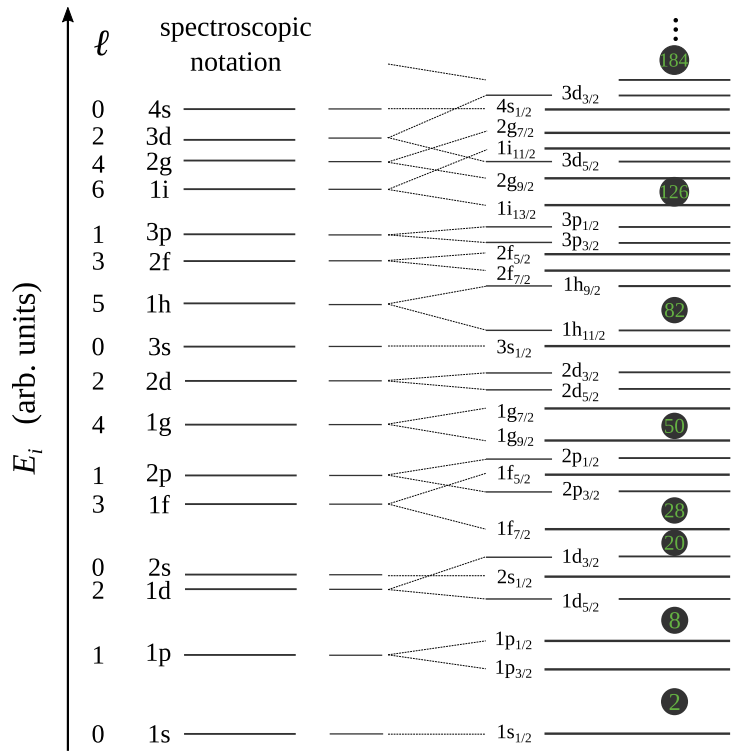


**Figure 4.1:** Single-particle energies $E_i$ obtained with a Woods-Saxon potential (left) and with a Woods-Saxon potential including the spin-orbit interaction (right). The resulting magic numbers are indicated by the circled numbers. Adopted from [3, 41].

Directly related to the $\ell$ quantum number is the parity $\pi = (-1)^\ell$ of a state. Hence, states in the $s$, $d$, $g$, $i$ orbitals have positive parity, and the $p$, $f$, $h$ orbitals have negative parity.

The energies $E_i$ are depicted on the left side of figure 4.1 and are labelled with the $n$ and $\ell$ quantum numbers of the corresponding wave functions. Each energy level is $2(2\ell + 1)$ degenerate, i.e. can be occupied by $2(2\ell + 1)$ particles. Since neutrons and protons are different particles, they are treated separately and can occupy the state at the same time. $^4$He, for example, has 2 neutrons as well as 2 protons in the $1s$ orbital.

As one can see, there are large gaps between the $1s$, $1p$ and $1d$ orbital, as well as between the $2s$ and $1f$ orbitals. These gaps correspond to 2, 8, and 20 occupied states, which reproduces the first three experimentally observed magic numbers. The magic numbers above 20, however, cannot be reproduced. It was found that the introduction of a *spin-orbit* interaction $V_{\ell s}\, \vec{\ell} \cdot \vec{s}$ solves this prob-

lem [42]. It partly lifts the degeneracy such that states with a high $j = \ell + \frac{1}{2}$ quantum number are lowered in energy, and those with lower $j = \ell - \frac{1}{2}$ are raised in energy. The effect is shown on the right hand side of 4.1, where the resulting energy levels are labelled according to their quantum numbers as $n\ell_j$. Each of these energy levels can be occupied by $2j + 1$ particles. The number of particles at the resulting energy gaps are indicated by the circled numbers and reproduce the experimental observation.
Having established such a shell structure, the ground state of a nucleus can be described by filling all the states with the available number of protons and neutrons, starting with the energetically lowest $1s$ orbital. An even number of protons (neutrons) will always tend to couple to spin 0, so that the odd valence proton (neutron) dictates the spin and parity of the ground state. An example for $^{127}$In is shown on the left hand side of figure 4.2. The neutrons are coupled to spin 0 whereas the valence proton in the $1g_{9/2}$ orbital is predicted to have a spin-parity $9/2^+$. Hence, the ground state of $^{127}$In has a spin-parity of $9/2^+$. Excited states are obtained if nucleons are excited to energetically higher lying states. However, it turns out that predicting the energies and spin-parities of excited states becomes rather difficult. The residual interaction cannot be neglected any more and the interaction of at least two nucleons needs to be taken into account. This is usually expressed by two-body matrix elements (TBME). Thereby, excited states are described as a mixture of several single-particle wave functions.
With increasing number of nucleons participating in the formation of excited states, the number of possible configurations for a state with a certain spin and parity increases drastically very quickly. In order to perform these calculations a number of shell-model computer codes have been developed. To reduce the complexity of the calculations, often an inert core (usually a doubly magic nucleus) is taken as a starting point, and the model space is defined by only a limited number of orbitals that are considered in the formation of excited states. The basic input for shell-model computer codes are so-called *interactions*, which are sets of single-particle energies (SPE) and TBMEs for the considered model space. There are numerous theoretical approaches to calculate these matrix elements, which are summarized and discussed, for example, in [43]. Often SPEs are also directly inferred from experiment.

## 4.2 NuShellX@MSU

In this work, the shell-model code NuShellX@MSU [44, 45] is used to calculate the level schemes of primarily $^{127}$In and $^{209}$Rn. Based on the chosen interaction

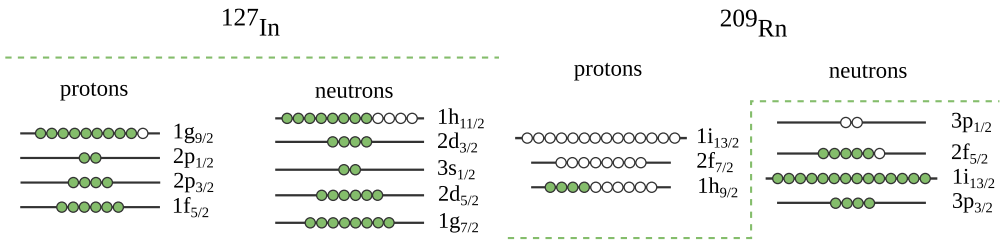


**Figure 4.2:** Considered orbitals in the shell-model calculations for $^{127}$In (left) and $^{209}$Ra (right). The green dashed line indicates the inert core, which is $^{132}$Sn in case of $^{127}$In and $^{208}$Pb in case of $^{209}$Rn.

and model space it calculates level energies as well as corresponding wave functions and lifetimes. It also provides the possibility to derive transition probabilities of electromagnetic transitions as well as Gamow-Teller strength distributions based on the calculated wave functions.
To calculate the energies and wave functions of $^{209}$Rn the '*pbpop*' interaction [46] was used, which is designed for nuclei around the doubly magic nucleus $^{208}$Pb. There, $^{208}$Pb is fixed as a closed core and the considered orbitals are $1h_{9/2}$, $2f_{7/2}$, and $1i_{13/2}$ for protons as well as $3p_{3/2}$, $1i_{13/2}$, $2f_{5/2}$, and $3p_{1/2}$ for neutrons, as depicted on the right side in figure 4.2. Results of the calculations are discussed in section 5.3 and in Paper II, section V.
Extensive calculations of the $^{127}$In decay scheme after the $\beta$ decay of the $11/2^-$ and $3/2^+$ states in $^{127}$Cd have been conducted. Here the '*NA-14*' [47] interaction was employed, which was already used in previous studies on the $\beta$ decay of $^{129}$Cd [48, 49] and other nuclei 'south-west' of $^{132}$Sn [50–52]. Not only the different states in $^{127}$In, but also the Gamow-Teller feeding into the excited states of $^{127}$In after the $\beta$ decay of $^{127}$Cd were calculated. Together with calculated reduced transition probabilities, $B(\sigma L)$ (see section 4.3), for all populated states in $^{127}$In, a decay scheme could be derived, which was then compared with the experimental observations. The results are discussed in detail in Paper III.

## 4.3 Electromagnetic transitions

If a nucleus is initially in an excited state, $\psi_i$, it can de-excite to a lower lying final state, $\psi_f$, by emitting the energy difference of these two states as a $\gamma$ ray or by internal conversion, i.e. ejecting an electron from the atomic shell. The character and multipole order of an electromagnetic transition are denoted $\sigma L$ and depend on the spins and parities, $J^\pi$, of the involved states, $J_i^{\pi_i}$ and $J_f^{\pi_f}$.

Since angular momentum must be conserved, $L$ has to fulfil

$$|J_f - J_i| \leq L \leq J_f + J_i.$$

Furthermore, a $\gamma$ ray has an intrinsic spin of 1, which implies that $L > 0$ for $\gamma$-ray transitions. The character, $\sigma$, of a transition is either *electric*, $E$, if $\pi_i\pi_f = (-1)^L$, or *magnetic*, $M$, for $\pi_i\pi_f = (-1)^{L+1}$.

The transition probability for a transition of type $\sigma L$ from the initial state $\psi_i$ to the final state $\psi_f$ with the energy difference $E_\gamma$ is expressed by the decay constant $\lambda(\sigma L, J_i \to J_f)$, which can be derived as

$$\lambda(\sigma L, \psi_i \to \psi_f) = \frac{8\pi(L+1)}{\hbar L((2L+1)!!)^2}\left(\frac{E_\gamma}{\hbar c}\right)^{2L+1} B(\sigma L, \psi_i \to \psi_f) \tag{4.4a}$$

$$B(\sigma L, \psi_i \to \psi_f) = \frac{1}{2J_i+1}|\langle \psi_i \parallel M(\sigma L) \parallel \psi_f\rangle|^2. \tag{4.4b}$$

Once the wave functions of the individual states have been calculated, shell-model codes such as NuShellX@MSU provide the possibility to determine the reduced matrix elements, $\langle \psi_i \parallel M(\sigma L) \parallel \psi_f\rangle$, and subsequently the reduced transition probabilities, $B(\sigma L, \psi_i \to \psi_f)$.
If there are $k$ final states $\psi_k$, then the branching ratio, $BR(\psi_i \to \psi_f)$, for a transition to a specific final state $\psi_f$ is given by

$$BR(\psi_i \to \psi_f) = \frac{\lambda(\psi_i \to \psi_f)}{\sum_k \lambda(\psi_i \to \psi_k)}. \tag{4.5}$$

Note that this in principle includes decay constants of particle decays such as $\alpha$ or $\beta$ decay as well. However, typically $E1$, $M1$, and $E2$ transitions are dominating.
Depending on the proton number, $Z$, of a nucleus as well as the transition energy and multipolarity, internal conversion might compete with the emission of a $\gamma$ ray. The probability of internal conversion is expressed by the inner conversion coefficient

$$\alpha_{ic} = \frac{\lambda_{ic}}{\lambda_\gamma}, \tag{4.6}$$

where $\lambda_{ic}$ and $\lambda_\gamma$ are electron and $\gamma$ transition rates, respectively. The conversion coefficients can be calculated quite accurately and are accessible, for instance, via the BrIcc database [53, 54]. In general, internal conversion becomes more

prominent the higher $Z$, the lower the transition energy, and the higher the multipole-order of the corresponding $\gamma$-ray transition. In the study of the $^{213}$Ra decay, internal conversion contributes significantly to the observed decay spectra as discussed in section 5.3 and in Paper II section IV. On the other hand, internal conversion is almost negligible in case of the $^{127}$In study.

## 4.4 $\beta$ decay

During a $\beta^-$ decay a neutron decays into a proton, an electron and an anti-neutrino. Hence, a nucleus of the element $X$ with mass number $A$, proton number $Z$, and neutron number $N$ decays into the element $Y$ with a proton number $Z+1$ and neutron number $N-1$,

$$\beta^- : \ {}^{A}_{Z}X_N \rightarrow \ {}^{A}_{Z+1}Y_{N-1} + e^- + \bar{\nu}_e.$$

Similarly, in a $\beta^+$ decay, a proton decays into a neutron, a positron and a neutrino,

$$\beta^+ : \ {}^{A}_{Z}X_N \rightarrow \ {}^{A}_{Z-1}Y_{N+1} + e^+ + \nu_e.$$

A third process called Electron Capture (EC), where an electron from the atomic shell is absorbed by the nucleus, competes with the $\beta^+$ decay,

$$EC : \ {}^{A}_{Z}X_N + e^- \rightarrow \ {}^{A}_{Z-1}Y_{N+1} + \nu_e.$$

The latter two processes play a role for nuclei on the proton-rich side of the valley of stability (marked red in figure 1.1). In heavier nuclei they often compete with the $\alpha$ decay, as it is the case, for instance, in $^{213}$Ra and its decay daughters. The $\beta^-$ decay, on the other hand, is the predominant decay mode for nuclei on the neutron-rich side of the valley of stability (marked blue in figure 1.1). Of particular interest in this work is the $\beta^-$ decay of $^{127}$Cd to $^{127}$In, which decays further until the stable $^{127}$I is reached (see figure 4.3).
Depending on the spin alignment of the emitted electron (positron) and anti-neutrino (neutrino), the $\beta$ decay is called Fermi decay if they are anti-parallel, i.e. coupled to total spin $S = 0$. If their spins are parallel and $S = 1$, one speaks about Gamow-Teller (GT) transitions. Furthermore, $\beta$ decays are categorized into *allowed* transitions, where the orbital angular momentum carried away by the emitted electron (positron) and anti-neutrino (neutrino) is $L = 0$, and *forbidden* transitions, where $L > 0$. Given that the parity of the electron wave function plus the neutrino wave function is $(-1)^L$, the parity of the nucleus

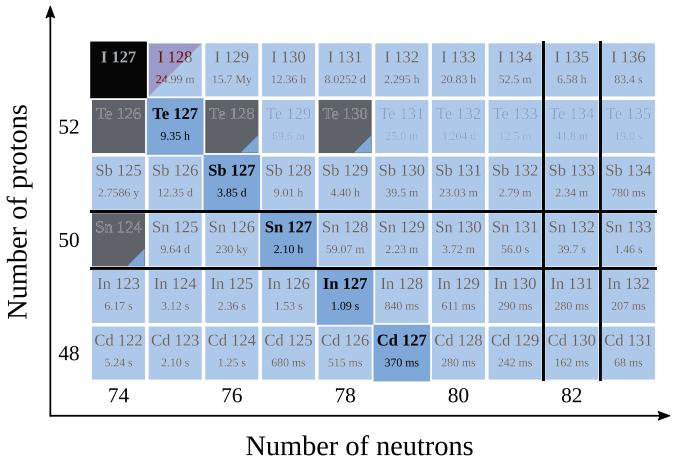


**Figure 4.3:** Excerpt from the nuclear chart [7] highlighting the $\beta$ decaying $^{127}$Cd, $^{127}$In, and subsequent daughter nuclei until the stable $^{127}$I is reached. Stable nuclei are marked black, $\beta^-$ decaying nuclei are marked blue and their ground-state half-lives are given. The magic number 50 for protons and 82 for neutrons are indicated by parallel black lines, with $^{132}$Sn being doubly magic.

does not change for allowed ($L = 0$) transitions as well as forbidden transitions where $L$ is even (e.g. second forbidden, $L = 2$). Consequently, for forbidden transitions where $L$ is odd (e.g. first forbidden, $L = 1$) the parities of the involved nuclear states must change. *Forbidden* transitions are not forbidden in a literal sense, but generally suppressed compared to allowed transitions.
When applying these classification rules to the model space considered for the $^{127}$Cd $\beta$ decay (cf. figure 4.2), it turns out that the $\nu 1g_{7/2} \rightarrow \pi 1g_{9/2}$ transition is the only allowed GT transition. Therefore one can expect that this transition dominates the $\beta$ decay of $^{127}$Cd. On the other hand, a number of first forbidden (ff) transitions are possible and might compete, leading to shorter half-lives of the decaying states. In case of nuclei with $N < 82$ and $Z < 50$ very close to doubly magic $^{132}$Sn, the strongest ff decays are the $\nu 1h_{11/2} \rightarrow \pi 1g_{9/2}$ and the $\nu 2d_{3/2} \rightarrow \pi 2p_{1/2}, 2p_{3/2}, 1f_{5/2}$ transitions. They are depicted in figure 4.4.

A first description of the $\beta$ decay was introduced by E. Fermi [55] and generalized by G. Gamow and E. Teller [56]. In the general case of a mixed Fermi and GT transition the decay constant for an allowed $\beta$ decay is

$$\lambda = \frac{m_e^5 c^4}{2\pi^3 \hbar^7} \, f(Q_\beta, Z) \, (g_V^2 \, B(F) + g_A^2 \, B(GT)\,), \tag{4.7}$$

where $g_V$ and $g_A$ are the vector and axial–vector coupling constants of the

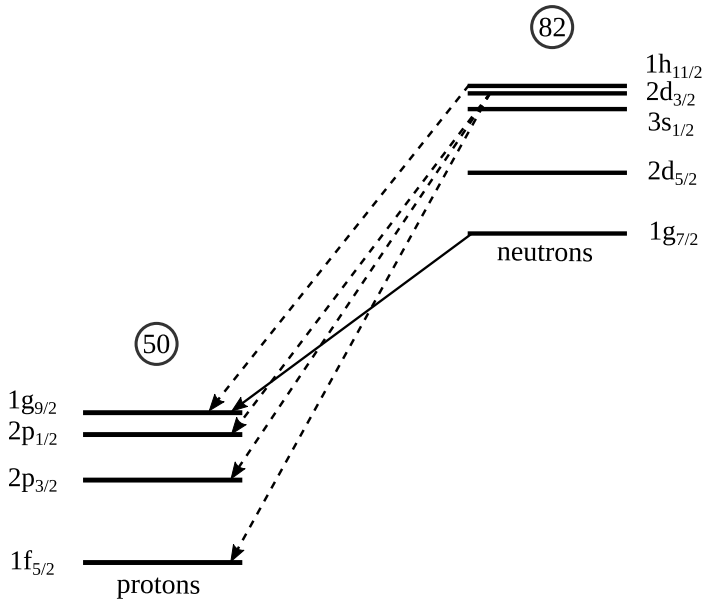


**Figure 4.4:** Allowed Gamow-Teller (solid) and most important first-forbidden (dashed) transitions within the considered model space for the shell-model calculations of the $^{127}$Cd $\beta$ decay. The shell gaps of the doubly magic $^{132}$Sn a indicated by the circled numbers.

weak interaction, and $f(Q_\beta, Z)$ the Fermi integral, which depends on the energy available for the decay, $Q_\beta$, and the proton number, $Z$, of the decaying nucleus. $B(F)$ and $B(GT)$ are the Fermi and GT transition strengths for the decay and depend on the initial and final nuclear state. However, usually the strength of a transition is expressed by the $ft$ value

$$ft = f(Q_\beta, Z)\frac{\ln 2}{\lambda} = \frac{2\,\ln 2\,\pi^3\hbar^7}{m_e^5 c^4\,(g_V^2\,B(F) + g_A^2\,B(GT)\,)}. \tag{4.8}$$

Similar to the case of the reduced matrix elements for $\gamma$-ray transitions, it is possible to calculate $B(F)$, $B(GT)$, and hence the $ft$ value with NuShellX@MSU, once the wave functions of the individual states have been calculated. The $ft$ value can be directly correlated to experimentally accessible observables

$$ft = \frac{I_\beta(E_f)}{f(Q_\beta, Z)\,T_{1/2}}, \tag{4.9}$$

where $I_\beta(E_f)$ is the direct $\beta$ feeding to the state at energy $E_f$ in the daughter nucleus, and $T_{1/2}$ the half-life of that decay. Note, that $Q_\beta$ depends on the

excitation energy of both the decaying state, $E_x$, as well as the final state, $E_f$. Hence, $Q_\beta = Q + E_x - E_f$, where $Q$ is the mass difference between the ground states of the mother and daughter nuclei. If these quantities have been experimentally determined, the online accessible LOGFT code [57] offers an easy way to calculate the $log\,ft$ value.
Since $ft$ values tend to become rather large and can have a wide range of values, often the $log\,ft$ value is used, rather than the $ft$ value itself. A distribution of experimentally observed $log\,ft$ values of known type is shown in figure 4.5. As one can see, forbidden transitions usually have $log\,ft$ values larger than 6, whereas the majority of allowed transitions have $log\,ft$ values between 4 and 8. Hence, the experimental determination of $log\,ft$ values can give direct insight on the type of $\beta$ decay and therefore on the underlying nuclear structure.

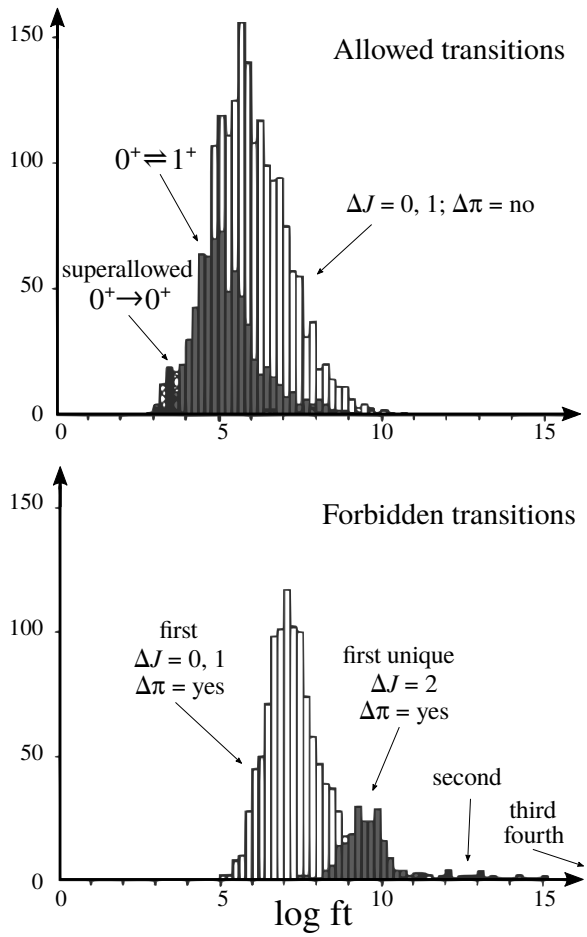


**Figure 4.5:** Distribution of experimentally observed $log\,ft$ values of allowed (upper panel) and forbidden (lower panel) transitions. Taken from [38].

# Chapter 5

# The Decay of $^{213}$Ra

In 2009 at the GSI Helmholtzzentrum für Schwerionenforschung in Darmstadt, Germany, an opportunity was given to probe the potential of the SHIPTRAP-TASISpec combination, using a so-called parasitic beam of $^{48}$Ca. The reaction $^{170}$Er($^{48}$Ca,5n)$^{213}$Ra was chosen on short notice and data of the $^{213}$Ra decay was taken for 15 h.
Thanks to the Penning trap SHIPTRAP (see section 2.3), the particles delivered to TASISpec are solely $^{213}$Ra ions without any contamination. This allows for a precise simulation not only of the detector response, but the whole experiment. Since the geometrical setup and its details are fixed and rather well known, the interaction of particles with matter well understood and implemented in GEANT4, the only free parameters in the simulation are the decay patterns of $^{213}$Ra and the produced daughter nuclei. Hence, if the results of a comprehensive and proper simulation are in significant disagreement with the experimental observation, then the decay patterns, i.e. the physics, specified for the simulation must be adjusted.

The experimental setup and the data processing prior to the physics analysis are explained in chapter 2 and chapter 3, respectively.
In this chapter, first a short description of the simulation of the decay and detection process using GEANT4 is given in section 5.1. Thereafter, the method for comparing simulation with experiment and deducing decay parameters such as $\alpha$-decay branching ratios is presented in section 5.2. The method and preliminary results are described in Paper I. The findings of this work have been published, discussed, and compared to theoretical calculations in Paper II. A short summary and some further details are provided in section 5.3.

## 5.1 GEANT4 Simulation of TASISpec

The GEANT4 framework [8, 9] is a toolkit for the simulation of the decay of particles and their interaction with matter. It is used in a wide range of fields, such as particle physics, nuclear physics, medical physics, and astrophysics. An important asset for this thesis is its proper simulation of the nuclear decay according to level schemes, decay channels, half-lives, and other nuclear properties specified in dedicated GEANT4 databases.
The decay spectroscopy setup TASISpec (see section 2.4) has been implemented in GEANT4 [58] and includes the possibility to easily adapt to changes of the setup in the different experiments where TASISpec was utilized. Such changes are, for example, number, type and positions of the used HPGe detectors, thickness and segmentation of the silicon detectors, and shape and position of the beam spot. The TASISpec simulation has already been used in a number of experiments to interpret the recorded data [59–65].
To simulate the decay and the detection of decay products of the $^{213}$Ra experiment, not only the geometry was adapted correspondingly but also the energy, rate and number of incoming $^{213}Ra^{2+}$ ions were taken into account. The beam profile was mimicked by a two-dimensional Gaussian which was tuned to reproduce the experimentally observed hit pattern in the implantation detector. As in the experiment, only one ion at a time is simulated whereas for the next simulated ion the internal clock is put forward by 400 ms, corresponding to the trap release cycle. Since the experiment was conducted for 15 h, the simulation of any particle which survived until that time was aborted. This plays a crucial role for the activity of the daughter nuclei produced by the $^{213}$Ra decay. The half-life of the $^{209}$Po ($T_{1/2} = 102(5)$ y) and $^{205}$Bi ($T_{1/2} = 15.31(4)$ d) daughter nuclei are much longer than the 15 h of experiment. Hence, they usually decay after the experiment was over. By including the proper trap cycle in the simulation and aborting the simulation after the experiment time is over, the amount of activity buildup during the experiment is properly taken care of, for all nuclei involved.
Energy depositions recorded in GEANT4 are added together if they are in prompt coincidence and in the same detector volume. Thereby the effect of energy summing is reproduced, which can explain deviations from the results obtained in this work from previously reported and evaluated results (see section 5.3 and Paper II section IV E). The intrinsic resolution of the silicon and HPGe detectors is modelled by convoluting the recorded energy deposition with a Gaussian distribution with the width corresponding to the measured energy resolution.
Each simulation run produces a list-mode file comprising energy, time and detector ID of each energy deposition, as it is the case in the experimental list-mode

data.
In the end it is possible to effectively perform a 'virtual' experiment including every aspect after the ions have left the Penning trap. One major requirement for this to be possible is the precise knowledge of the beam, which is provided by the selection of only $^{213}Ra^{2+}$ ions with SHIPTRAP.

## 5.2 Simulation versus Experiment

In order to efficiently simulate and compare experiment and simulation a semi-automatized routine using ShellScript, C++, and the ROOT framework [30, 31] has been developed.

The output from the simulation is fed into the same list-mode analysis code which was used to analyse the experimental data (see chapter 3), so that both experiment and simulation are analysed the exact same way. This includes in particular add-back algorithms and the coincidence analysis between photons and particles. The produced output file contains photon, particle, and photon-particle coincidence spectra.
The only difference concerning the analysis of the simulation is the energy calibration. Since the simulation provides the exact energy that has been deposited in a detector volume, there is in principle no energy calibration needed. In the experiment, the HPGe detectors can be calibrated quite accurately (see chapter 3) and so this should not be a concern. The energy calibration of the silicon detectors, however, strongly depends on its dead-layer thickness, which often is not known very precisely. Therefore, the experiment has been calibrated assuming a dead layer of 1.6 $\mu$m. In the simulation, the dead layer thickness was treated as a free parameter. When changing the dead-layer thickness in the simulation, the detected particle energies and therefore the peak positions in the particle spectrum vary for each different dead-layer thickness. To be able to compare the shape of simulated particle spectra with the experiment, each simulated spectrum has been automatically 'recalibrated' so that it fits the experimental calibration. This has been achieved by using equation 5.1 [66] to approximate the experimental and simulated particle spectra shape. There, $n$ is the number of peaks in the spectrum, $I_k$ the measure of their areas and $\mu_k$ their respective peak positions. The shape of the peak is given by the weight and tailing parameters $\eta_i$, $\eta_{tot} = \sum_{i=1}^{3} \eta_i$ and $\tau_i$ of the exponentials as well as the standard deviation of the Gaussian, $\sigma$. Note that the shape parameters are the same for all peaks. The obtained peak positions $\mu_k$ have then been used to deduce a linear calibration for the simulation. The fit is demonstrated in figure 5.1(a).

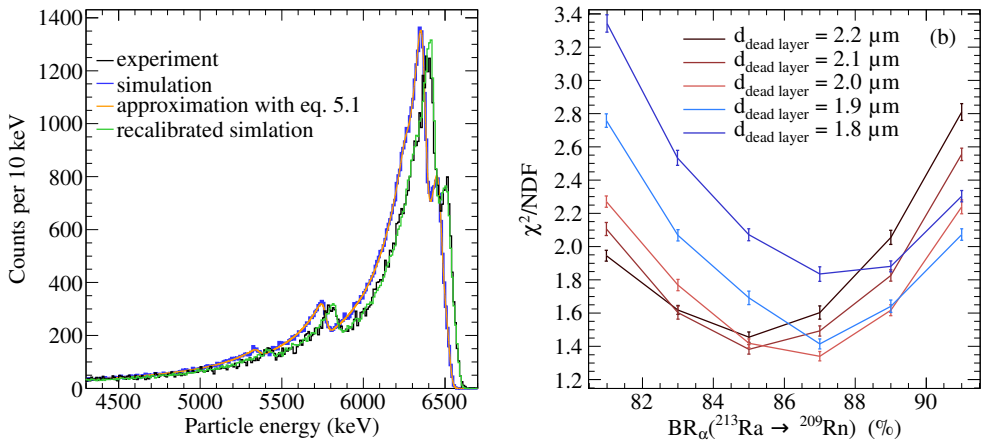


**Figure 5.1:** (a) An example of a simulated particle spectrum in comparison with the experiment. To be able to compare them by means of a $\chi^2$-test, the simulated spectrum is approximated with equation 5.1, recalibrated, and normalized to the experimental yield.
(b) The change of the reduced $\chi^2$ for varying dead-layer thickness and total $\alpha$-decay branching-ratios of $^{213}$Ra. Best agreement with experiment is obtained for a dead-layer thickness between 1.9 and 2.1 $\mu$m and a total $\alpha$-decay branching-ratio around 86 %.

$$f(E) = \sum_{k=1}^{n} \frac{I_k}{3} \left\{ \sum_{i=1}^{3} \frac{\eta_i}{\eta_{tot}\tau_i} \exp\left( \frac{E-\mu_k}{\tau_i} + \frac{\sigma^2}{2\tau_i^2} \right) \operatorname{erf}\left( \frac{1}{\sqrt{2}} \left[ \frac{E-\mu_k}{\sigma} + \frac{\sigma}{\tau_i} \right] \right) \right\} \quad (5.1)$$

Another rather uncertain variable is the exact number of implanted $^{213}$Ra ions (see section 2.1). A variation in the number of implanted ions in the simulation obviously alters the yield in every spectrum. Changing the dead-layer thickness has a similar effect: the thinner the dead layer, the easier it is for $\alpha$ particles to reach the active detector volume and vice versa. To compensate for that, every simulated particle spectrum has been normalized to the experimentally observed one. An example of the recalibrated and normalized particle spectrum is shown in figure 5.1(a). The obtained normalization factor was then used to also normalize the photon and coincidence spectra from the same simulation. If all $\alpha$-decay branching ratios are correct, then the obtained yields in the simulated histograms should be accurately reproduced after the normalization with this single common factor.
To compare the shape of histograms from simulation and experiment a $\chi^2$-test was used [67]. The closer the obtained reduced $\chi^2$ is to a value of unity, the

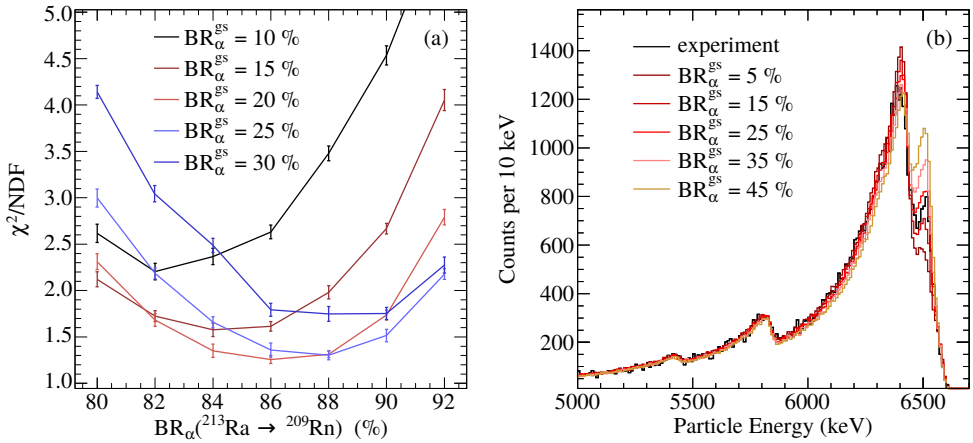


**Figure 5.2:** (a) The change in the reduced $\chi^2$ of the particle spectrum for varying total $\alpha$-decay branching-ratios, $BR_\alpha$, of the $^{213}$Ra decay and relative branching ratios to the ground state of $^{209}$Rn. (b) The average simulated particle spectra for a total $^{213}$Ra $\alpha$-decay branching-ratio of 87 % and varying $\alpha$-decay branching-ratios to the ground state of $^{209}$Rn in comparison with the particle spectrum from the experiment.

better the compared histograms agree. Before calculating the $\chi^2$ for a simulated histogram, it was normalized to the corresponding experimental histogram, so that the $\chi^2$ value contains only information about differences in the shape and not in the yield of the histograms.

In order to obtain a measure for the sensitivity of an observable (e.g. $\chi^2$-values, normalization factors) when parameters are varied, each parameter set is simulated 10 to 30 times. After all runs of a parameter set are analyzed, the mean and standard deviation of each observable are estimated.

When a batch of simulations with varying input parameters has been run, automatically analyzed and compared with the experiment, the results, for instance the resulting histograms, graphs with normalization factors, and $\chi^2$ values as function of the varied input parameters, were stored in the ROOT file format. After manually inspecting the results and deciding on new input parameters, the next batch of simulations were started. The range of a parameter as well as the number of points in that range were specified in a ShellScript which then would automatically create the necessary input files for GEANT4 and start the simulations. When varying, for example, the $\alpha$-decay branching ratio for the decay of $^{213}$Ra to the ground state of $^{209}$Rn, the script would also normalize the $\alpha$-decay branching-ratio to the exited states of $^{209}$Rn so that their sum would amount to 100%.

As is shown in Papers I (figure 3(a)) and II (figure 3), it is not possible to reproduce the experimental spectra using the evaluated data of the $^{213}$Ra decay path [68–70]. In the following, the process of determining the parameter set that reproduces the experimental observation best is exemplified on results from various simulations around the final and published parameter set.
Figure 5.1(b) shows the change of the reduced $\chi^2$ when varying the total $^{213}$Ra $\alpha$-decay branching-ratio and the dead-layer thickness at the same time. As mentioned previously, the uncertainty bars indicate the variation of the reduced $\chi^2$ value when simulating the same parameter set several times. One can see that a dead layer thinner than 1.9 $\mu$m very quickly leads to much worse $\chi^2$ values. Also dead layers thicker than 2.1 $\mu$m result in significantly worse reduced $\chi^2$ values than a dead-layer thickness of 2.0 $\mu$m which leads on average to the most consistent reproduction of the experiment. This is in good agreement with the dead-layer thickness determined for similar DSSSD detectors used for other experiments with TASISpec [33].

Similarly the intrinsic detector resolution of the silicon detectors in the simulation has been varied. However, its effect on the final result turned out to be negligible, compared to the effect due to the dead layer. This can be easily understood by estimating the energy loss of the $\alpha$ particles when passing through the dead-layer: as mentioned in section 2.4, the $^{213}$Ra ions had kinetic energy of only 3 keV. Using SRIM [71] to simulate the implantation of 3 keV $^{213}Ra^{2+}$ ions into $SiO_2$ (the dead layer material; taken from the standard compound dictionary of SRIM), one obtains an 'implantation depth' of $\sim 7$ nm. This is insignificantly small compared to the dead-layer thickness, which is on the order of micrometers. Hence, the $\alpha$ particles have to traverse effectively the whole dead layer before reaching the active detector volume where they can be detected. Depending on the emission angle during the $\alpha$ decay, the path length through the dead-layer material varies, leading to a significant tail on the low energy side of the $\alpha$ peaks (see figure 5.2(b)). For example, a 7 MeV $\alpha$ particle loses $\approx 250$ keV in 2.0 $\mu$m $SiO_2$. If such an $\alpha$ particle did not go straight through the 2.0 $\mu$m dead-layer, but in an angle of e.g. 25°, it has to traverse 2.2 $\mu$m. This corresponds to an energy loss of around 280 keV, i.e. 30 keV more than an $\alpha$ particle that goes straight through the dead layer. An $\alpha$ particle emitted at an angle of 45° loses $\sim 100$ keV more. This is more than the intrinsic detector resolution of silicon detectors which is around 20 to 25 keV at 7 MeV. Since the $\alpha$ particles are emitted isotropically, the dead layer has a stronger effect on the final resolution of the particle spectrum than the intrinsic detector resolution.
Another example is shown in figure 5.2, where the $^{213}$Ra $\alpha$-decay branching-ratio to the $^{209}$Rn ground-state has been varied. Similar to figure 5.1(b), figure 5.2(a) shows the change of the reduced $\chi^2$ when varying the total $^{213}$Ra

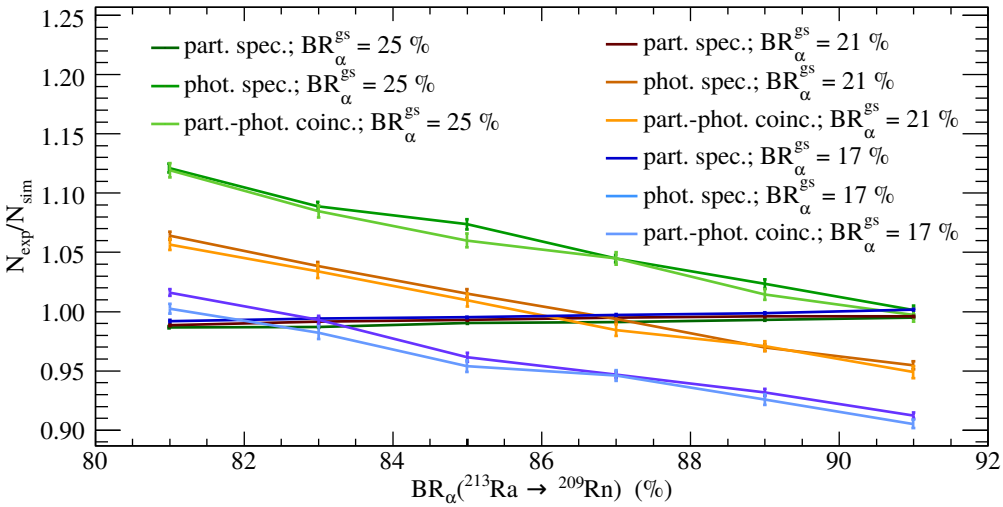


**Figure 5.3:** The normalization factors for simulated particle, photon, and particle-photon coincidence spectra for varying total $\alpha$-decay branching ratios of the $^{213}$Ra decay and relative branching ratios to the ground state of $^{209}$Rn, $BR_\alpha^{gs}$.

$\alpha$-decay branching-ratio and relative branching ratio to the $^{209}$Rn ground-state at the same time. It is obvious from this graph as well as from the spectra shown in figure 5.2(b) that the evaluated values for the $\alpha$-decay branching-ratios of 80 % and 46 %, respectively, lead to significant discrepancies between simulation and experiment. Investigating figure 5.2(a) reveals that these branching-ratios are around 86 to 88 % and between 20 and 25 % respectively. On average a total $\alpha$-decay branching-ratio of 86 % and a relative $\alpha$-decay branching-ratio of 20 % lead to similarly good results as branching ratios of 88 % and 25 %.

The graphs shown in figures 5.1(b) and 5.2(a) provide information about the $\alpha$-decay branching-ratios based on the particle spectrum. For photon spectra however, the $\chi^2$ does not change when only varying the total $\alpha$-decay branching-ratio and the relative $\alpha$-decay branching-ratio to the $^{209}$Rn ground-state, because the relative intensities of the $X$-ray and $\gamma$-ray peaks do not change. What changes, however, are the yields of the photon and particle-photon coincidence spectra. This can be visualized by the different normalization factors that are needed to obtain the same yields in the simulated spectra as in the corresponding experimental spectra. An example is shown in figure 5.3. There one can see that the normalization factors for the particle spectrum are rather constant, in contrast to the $\chi^2$ values of the particle spectrum as discussed previously. The normalization factor for the photon spectrum, and therefore for the coincidence spectrum as well, is larger for lower total $\alpha$-decay branching-ratios and

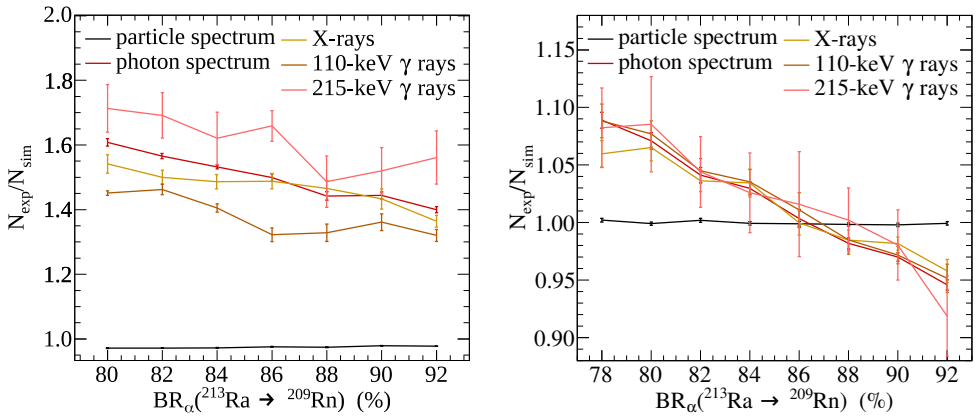


**Figure 5.4:** Normalization factors for the particle and the photon spectrum as well as the $X$-ray, 110-keV and 215-keV $\gamma$-ray intensities when using (a) the evaluated decay data and (b) the revised decay data for the $^{213}$Ra decay as input for the GEANT4 simulation.

for larger relative $\alpha$-decay branching-ratios to the $^{209}$Rn ground-state. This is not surprising since in both cases the feeding into the exited states of $^{209}$Rn is decreased. As mentioned earlier, a consistent reproduction of the experimental observation implies that the three spectra have the *same* normalization factors. When simulating a relative $\alpha$-decay branching-ratio to the $^{209}$Rn ground-state of 25 %, then the total $\alpha$-decay branching-ratio of $^{213}$Ra needs to be around 91 % in order to reproduce the correct yields in the photon and particle-photon coincidence spectra. However, looking at the corresponding $\chi^2$ values of the particle spectrum in figure 5.2(a), one observes that the reduced $\chi^2$ value is rather bad, i.e. the shape of the simulated particle spectrum does not agree well with experiment. Similarly for a relative ground-state $\alpha$-decay branching-ratio of 21 %, the total $\alpha$-decay branching-ratio should be 87 %, which in turn fits well to the corresponding reduced $\chi^2$ value (compare to $\mathrm{BR}_\alpha^{\mathrm{gs}} = 20\,\%$ in figure 5.2(a)).

In figure 5.4 one can nicely compare the normalization factors for the evaluated decay data, figure 5.4(a), and the revised decay data, figure 5.4(b). It is obvious that the photon yield is greatly underestimated when using the evaluated decay data to simulate the $^{213}$Ra decay. Furthermore, the average normalization factors for $X$ rays, 110-keV, and 215-keV $\gamma$ rays are slightly different. Hence the relative $\alpha$-decay branching-ratios into the excited states of $^{209}$Rn have to be adjusted.

Figure 5.5(a) shows the intensity differences of the $\gamma$-ray peaks for varying relative $\alpha$-decay branching-ratios to the first excited state of $^{209}$Rn. Naturally, lowering this relative $\alpha$-decay branching-ratio leads to an underestimation of

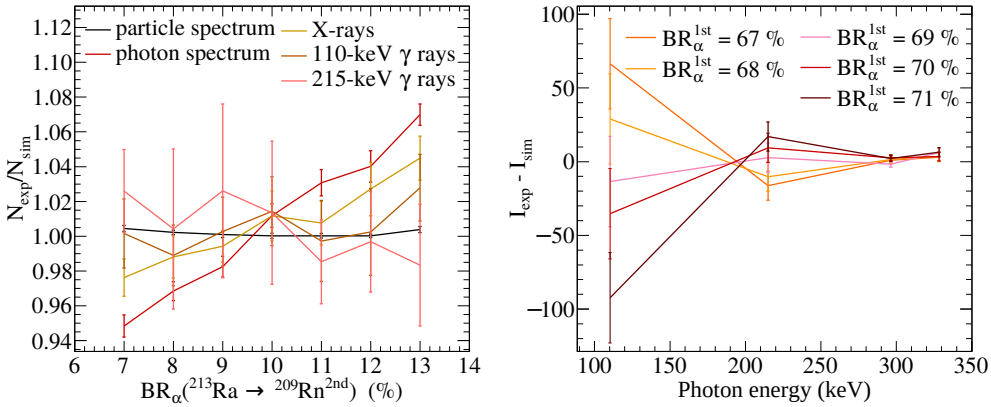


**Figure 5.5:** (a) Difference of experimental and simulated peak intensities when varying the relative $\alpha$-decay branching-ratio to the first excited state of $^{209}$Rn, $\mathrm{BR}_\alpha^{1\mathrm{st}}$. (b) Normalization factors for the particle and the photon spectrum as well as the $X$-ray, 110-keV, and 215-keV $\gamma$-ray intensities when varying the relative $\alpha$-decay branching ratio to the second excited state of $^{209}$Rn.

the 110-keV peak intensity. At the same time the 215-keV peak intensity is overestimated, because the relative $\alpha$-decay branching-ratios to the other states in $^{209}$Rn have to be increased at the same time to sum up to 100 %. Good agreement is achieved for a relative $\alpha$-decay branching ratio to the first excited state between 68 % and 69 %, which is an increase by a factor of 1.4 compared to the evaluated data.

In figure 5.5(b) the relative $\alpha$-decay branching ratio to the second excited state of $^{209}$Rn is varied. On average, the intensity of the 215-keV peak changes from slightly overestimated to slightly underestimated if the branching ratio is increased. However, as one can see these intensities vary significantly if the simulations are repeated with the same branching ratio. Therefore, the yield of the 215-keV peak is not a decisive indicator to narrow down the relative $\alpha$-decay branching ratio to the second excited state as one might expect. On the other hand, when increasing the $\alpha$-decay branching-ratio to the second excited state, one decreases at the same time the $\alpha$-decay branching-ratios to the other excited states, most importantly to the first one. This results in a significant change of yields in the total photon spectrum, with an opposite trend compared to the 215-keV peak intensity. For a relative $\alpha$-decay branching ratio to the second excited state between 9 % and 10 % all normalization factors agree best, such that this $\alpha$-decay branching-ratio is slightly more increased than the relative $\alpha$-decay branching-ratio to the first excited state. Thereby it was possible to adjust the relative $\alpha$-decay branching-ratios to the excited states in a way that the same

average normalization factors are obtained for the total photon spectrum, the $X$-ray, 110-keV and 215-keV $\gamma$-ray intensities.

## 5.3 Results and Theoretical Interpretation

After performing a great number of simulations and thereby developing the routine described in the previous section 5.2, a much better agreement between simulation and experiment could be achieved, essentially by modifying $\alpha$-decay branching ratios of $^{213}$Ra. As discussed in Paper II, the hitherto assigned multipolarities for the $\gamma$-ray transitions de-exciting the first and second excited states in $^{209}$Rn can be confirmed. Due to low statistics, however, significant constraints on relative $\gamma$-ray intensities could not be achieved.
An explanation as to why the obtained $\alpha$-decay branching ratios differ so significantly compared to the evaluated data is the summing effect of $\alpha$-particle energies and conversion-electron energies. This is discussed in Paper II, section IV E. Albeit the general opinion about studies which involve simulations to such extent are rather sceptical, the results from this work are in much better agreement with theoretical calculations. This holds especially for the $\alpha$-decay branch to the ground state (see Paper II). The theoretical calculations for the relative $\alpha$-decay branching ratios from the $^{213}$Ra ground state into the $^{209}$Rn ground-state, the first and second excited states were performed by D. Ward [72, 73]. These calculations are based on the overlap of the wave functions from initial and final state and assume single particle states as well as a spherical nucleus.
To justify the assumption of single-particle states, shell-model calculations have been conducted with the NuShellX@MSU code (cf. chapter 4). Predicted level energies of yrast states for $N = 123$ and $N = 125$ odd-mass nuclei neighbouring $^{209}$Rn and $^{213}$Ra are shown in figure 5.6 and compared to the corresponding experimental results [68–70, 74–76].
All the calculations were conducted as described in section 4.2. For $^{211}$Ra and $^{215}$Th, however, the dimensions of the matrices to be diagonalized by NuShellX@MSU routines approached the computational limits. Hence, the calculations had to be restricted, such that number of protons occupying the $2f_{7/2}$ and $1i_{13/2}$ is limited to two. Thereby it was possible to calculate the $1/2^-$ and $3/2^-$ yrast states for $^{215}$Th as well as the $1/2^-$, $3/2^-$, $5/2^-$ and $13/2^+$ yrast states for $^{211}$Ra.

The calculations predict energies and spin sequence of the low lying states with negative parity intriguingly well. A ground-state spin-parity $1/2^-$ is predicted for the $N = 125$ isotones $^{209}$Po, $^{211}$Rn, $^{213}$Ra, and $^{215}$Th, in accordance

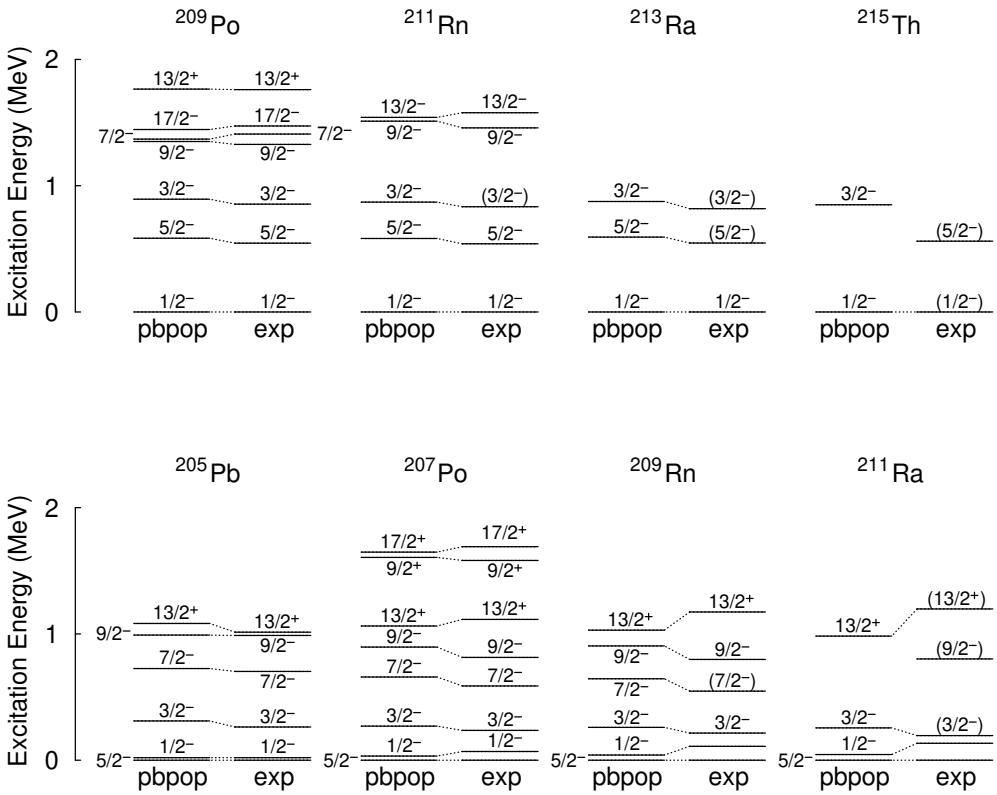


**Figure 5.6:** Yrast states for the $N = 123$ (lower panel) and $N = 125$ (upper panel) odd-mass nuclei neighbouring $^{209}$Rn and $^{213}$Ra calculated with NuShellX@MSU using the pbpop interaction (see section 4.2) in comparison with the corresponding experimental observations [68–70, 74–76]. Tentative spin and parity assignments are shown in parentheses.

with experiment. These states are dominated by $\nu(3p_{1/2})^{-1}$ configurations, which contribute over 90 % to the ground-state wave functions of these nuclei. Similarly, the first and second excited states are dominated by $\nu(2f_{5/2})^{-1}$ and $\nu(3p_{3/2})^{-1}$ configurations, respectively, contributing between 80 % and 90 % to the ground-state wave functions.

In case of the $N = 123$ isotones $^{205}$Pb, $^{207}$Po, $^{209}$Rn, and $^{211}$Ra, the correctly predicted $5/2^-$ ground states are dominated by $\nu(2f_{5/2})^{-1}$ configurations. The contribution of such partitions to the ground-state wave functions ranges from 100 % in $^{205}$Pb to 81 % in $^{211}$Rn. Likewise, the first and second excited states are

**Table 5.1:** Experimental and theoretical excitation energies, $E_x$, branching ratios, $b$, and $\gamma$-ray branching ratios, $b_\gamma$ as well as the calculated lifetimes, $\tau_{theo}$. The inner conversion coefficients, $\alpha_{tot}$, are obtained from [53, 54] using the transition energies, $E_\gamma$, observed in the experiment, and pure $M1$ and $E2$ transitions.

| $E_{x,exp}$ (keV) | $E_{x,theo}$ (keV) | $\tau_{theo}$ | $J_i^\pi$ ($\hbar$) | $J_f^\pi$ ($\hbar$) | $E_\gamma$ (keV) | $b_{\gamma,exp}$ (%) | $b_{\gamma,theo}$ (%) | $\alpha_{tot}$ [53, 54] | $b_{exp}$ (%) | $b_{theo}$ (%) |
|---|---|---|---|---|---|---|---|---|---|---|
| 110 | 41 | 2.0 $\mu$s | $1/2_1^-$ | $5/2_1^-$ | 110.6(2) | 100 | 100 | 5.41(9) | 100 | 100 |
| 215 | 260 | 79 ps | $3/2_1^-$ | $1/2_1^-$ | 106(1) | 24(5) | 45 | 11.1(4) | 60(9) | 80 |
| | | | $3/2_1^-$ | $5/2_1^-$ | 215.2(2) | 76(5) | 56 | 1.5(3) | 40(9) | 20 |
| 328 | 466 | 37 ps | $3/2_2^-$ | $3/2_1^-$ | 113.3(2) | $< 12$ | 0.2 | 9.2(2) | $< 44$ | 10 |
| | | | $3/2_2^-$ | $1/2_1^-$ | 218.1(2) | 29(14) | 71 | 1.4(2) | $> 25$ | 73 |
| | | | $3/2_2^-$ | $5/2_1^-$ | 328.3(1) | 59(18) | 27 | 0.47(7) | $> 31$ | 17 |

constituted primarily by $\nu(3p_{1/2})^{-1}$ and $\nu(3p_{3/2})^{-1}$ configurations, with contributions of 100 % and 100 % in $^{205}$Pb to 83 % and 76 % in $^{211}$Rn, respectively. The overall good reproduction of the level energies and sequence of the $1/2^-$, $3/2^-$, and $5/2^-$ states in particular, justifies the assumption of single-particle states in the calculations for the relative $\alpha$-decay branching ratios, which are discussed in Paper II section V.

In addition, reduced transition probabilities of $M1$ and $E2$ transitions in $^{209}$Rn were calculated with NuShellX@MSU. Here, standard effective charges, $e_{eff,p} = 1.5$ and $e_{eff,n} = 0.5$, and unquenched, free $g$ factors are used. Together with experimental transition energies, transition rates, branching ratios, $b_{theo}$, and lifetimes, $\tau_{theo}$, could be derived using equation 4.4a. Furthermore, $\gamma$-ray branching ratios, $b_{\gamma,theo}$, can be inferred by correcting for predicted conversion coefficients [53, 54]. The results are shown in table 5.1 together with the experimental observations. In the experiment the $3/2_1^-$ state at 215 keV is predicted to primarily decay into the first excited $1/2^-$ state. In case of the $3/2_2^-$ 328 keV state, the comparison is somewhat hampered due to rather large experimental uncertainties. Finally, the 110 keV state is predicted to be an isomer with a half-life of $T_{1/2,theo} = 1.4\mu$s. From the time distribution of the 110 keV $\gamma$ rays observed in the experiment, a half-life of $T_{1/2,exp} = 59(5)$ ns could be deduced. The corresponding time distribution is shown in figure 5.7, approximated with equation 2.1.

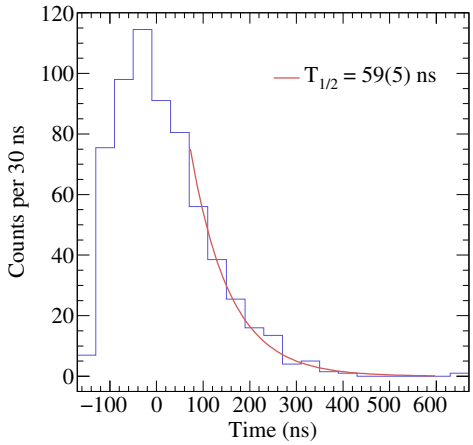


**Figure 5.7:** Time distribution of 110 keV $\gamma$ rays with respect to the particle trigger observed in the experiment and its approximation with an exponential decay function.

# Chapter 6

# $^{127}$Cd

The experiment to study the decay properties of $^{127}$Cd was conducted in 2017 at the Ion Guide Isotope Separation On-Line (IGISOL) facility at the University of Jyväskylä. Motivation for this experiment was to study the hitherto experimentally unresolved evolution of the $11/2^-$ neutron-hole isomer along the chain of odd-mass cadmium isotopes for $A = 127$ and 129. The spins of the two long lived states in the odd-mass $^{121-129}$Cd isotopes were measured to be 11/2 and 3/2 by Yordanov *et al.* [77]. However, the order of these states has not been determined experimentally for any of these isotopes. Following the systematic trends in lighter cadmium isotopes in combination with measured $log\ ft$ values for some of these isotopes, one rather firmly identifies the $11/2^-$ state as the isomer and the $3/2^+$ state as the ground state in case of the $^{121,123,125}$Cd isotopes [21, 78, 79]. Between $^{127}$Cd and $^{129}$Cd a crossing of these two states is predicted by shell-model calculations [49].

Assuming a rather well known decay scheme of $^{127}$In ($^{129}$In), which is populated after the $\beta$ decay of $^{127}$Cd ($^{129}$Cd), it is possible to correlate emitted $\gamma$ rays with the $\beta$ decay of either the $3/2^+$ or the $11/2^-$ state in $^{127}$Cd ($^{129}$Cd). With the mass resolving power of JYFLTRAP it is possible to separate the ground and isomeric states (see section 2.3.3), and study their $\beta$ decay and emitted $\gamma$ rays individually. Thereby it is possible to unambiguously correlate the spin-parity $3/2^+$ or $11/2^-$ (via the detected $\gamma$ rays) to either ground state or isomer, depending on what was selected by the Penning trap. Although this method proved to be in principle feasible, the rate of delivered ions was too low to obtain significant $\gamma$-ray spectroscopy information. The outcome of such an attempt using the phase-dependent cleaning method to separate and uniquely study the isomer of $^{127}$Cd is discussed in section 6.3.

By omitting the separation of ground and isomeric states, hence using a mixed beam containing both isomeric and ground state of $^{127}$Cd, it was possible to collect sufficient statistics to considerably extend the decay scheme of $^{127}$In, identify $\gamma$-ray transitions in $^{127}$In which are characteristic for the $\beta$ decay of either the $3/2^+$ or the $11/2^-$ state in $^{127}$Cd, and investigate the $\beta$-decay feedings into the excited states of $^{127}$In. Despite of having the isomeric and ground states of $^{127}$Cd mixed in the incoming beam, it was still possible to identify the $11/2^-$ state in $^{127}$Cd as the isomer of $^{127}$Cd. Furthermore, extensive shell-model calculations as described in chapter 4 have been conducted and confronted with the experiment. These findings are presented and discussed in Paper III. The experimental setup is shown in chapter 2 and the data processing is detailed in chapter 3. This chapter summarizes and adds to the discussion of the results presented in Paper III.

## 6.1 The $^{127}$In decay scheme

Previous to this study 43 $\gamma$-ray transitions had been associated with the $\beta$ decay of $^{127}$Cd to $^{127}$In, but only 18 were placed in a level scheme consisting of 14 excited states [22, 80, 81]. To independently identify $\gamma$-ray transitions in $^{127}$In the observed $\gamma$ rays have been sorted into *signal* and *background* spectra according to their time relative to the last trap release signal as depicted in figure 6.1(a). There a numerical estimate of the average activity of $^{127}$Cd and the first two daughter nuclei during a $\sim 140$ ms trap cycle is shown and the *signal* and *background* regions are indicated. The decays of the daughter nuclei are not correlated with the trap release at $t_\gamma - t_{\text{release}} = 0$ and their half-lives are much longer than the trap cycle. Together with the very low deposition rate of seven to ten $^{127}$Cd ions per second (i.e. $\sim 1.2$ ions per cycle), this leads to on average constant daughter activity during a trap cycle. The activity of $^{127}$Cd, however, is correlated to the latest trap release, since new $^{127}$Cd ions are deposited on the catcher foil with every trap release. Due to the rather short half-life of $^{127}$Cd, its activity is significantly lower in the *background* region than in the *signal* region. During the experiment no data was recorded 1 ms and 11 ms after a trap release, which was discussed in section 3.3, which falls into the *signal* region. Therefore, the *signal* spectrum was normalized such that the intensity of the 490 keV peak is the same as in the *background* spectrum. This peak stems from the $\beta$ decay of $^{127}$Sn into $^{127}$Sb. Hence, its activity during a trap cycle is constant and its intensity must therefore be the same in the *signal* and the *background* spectrum. The resulting spectra are shown in figure 6.1(b). One can clearly see that the $\gamma$-ray peaks originating from the $^{127}$Cd $\beta$ decay

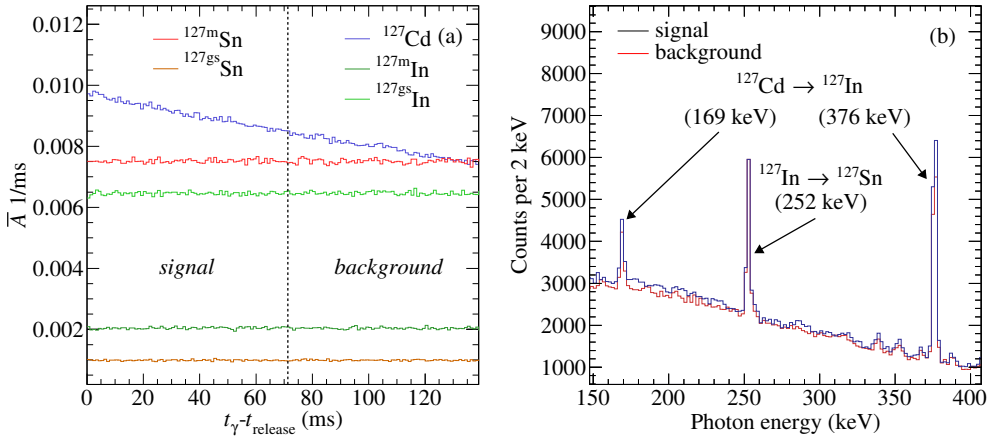


**Figure 6.1:** (a) Numerically estimated average activity during a 140 ms trap cycle of $^{127}$Cd as well as the isomeric and ground states of the first two daughters $^{127}$In and $^{127}$Sn. The measured $\gamma$-ray spectra obtained from events that are detected within the first 70 ms of a trap cycle, the *signal* region, and from those that are detected within the last 70 ms of a trap cycle, the *background* region, are shown in panel (b).

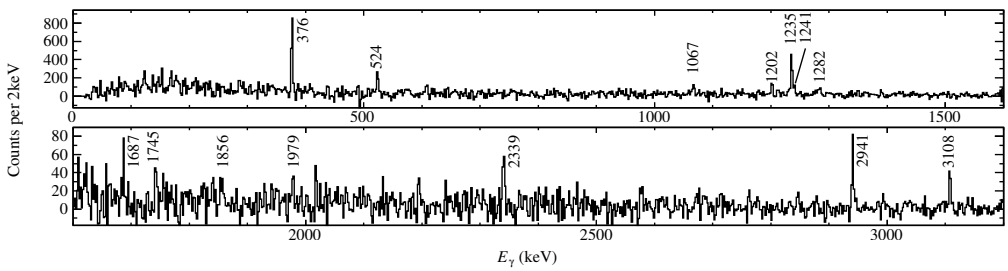


**Figure 6.2:** Resulting spectrum when subtracting the *background* spectrum from the *signal* spectrum (cf. figure 6.1). The observed $\gamma$-ray peaks can be firmly associated with the transitions in $^{127}$In, populated after the $^{127}$Cd $\beta$ decay. Spectrum taken from Paper III.

are more intense in the *signal* spectrum, whereas the 252 keV peak from the $\beta$ decay of $^{127}$In is the same in both spectra. Subtracting the $\gamma$-ray spectrum of the *background* region from the *signal* region results therefore in a spectrum containing only $\gamma$-ray peaks originating from the $^{127}$Cd $\beta$ decay, which is show in figure 6.2. This way a number of already known $\gamma$-ray transitions in $^{127}$In could be confirmed, for example the very prominent 376 and 1235 keV transitions associated with the $\beta$ decay of the $^{127}$Cd $11/2^-$ state and the 524 keV transition, which populates the $^{127}$In isomer.

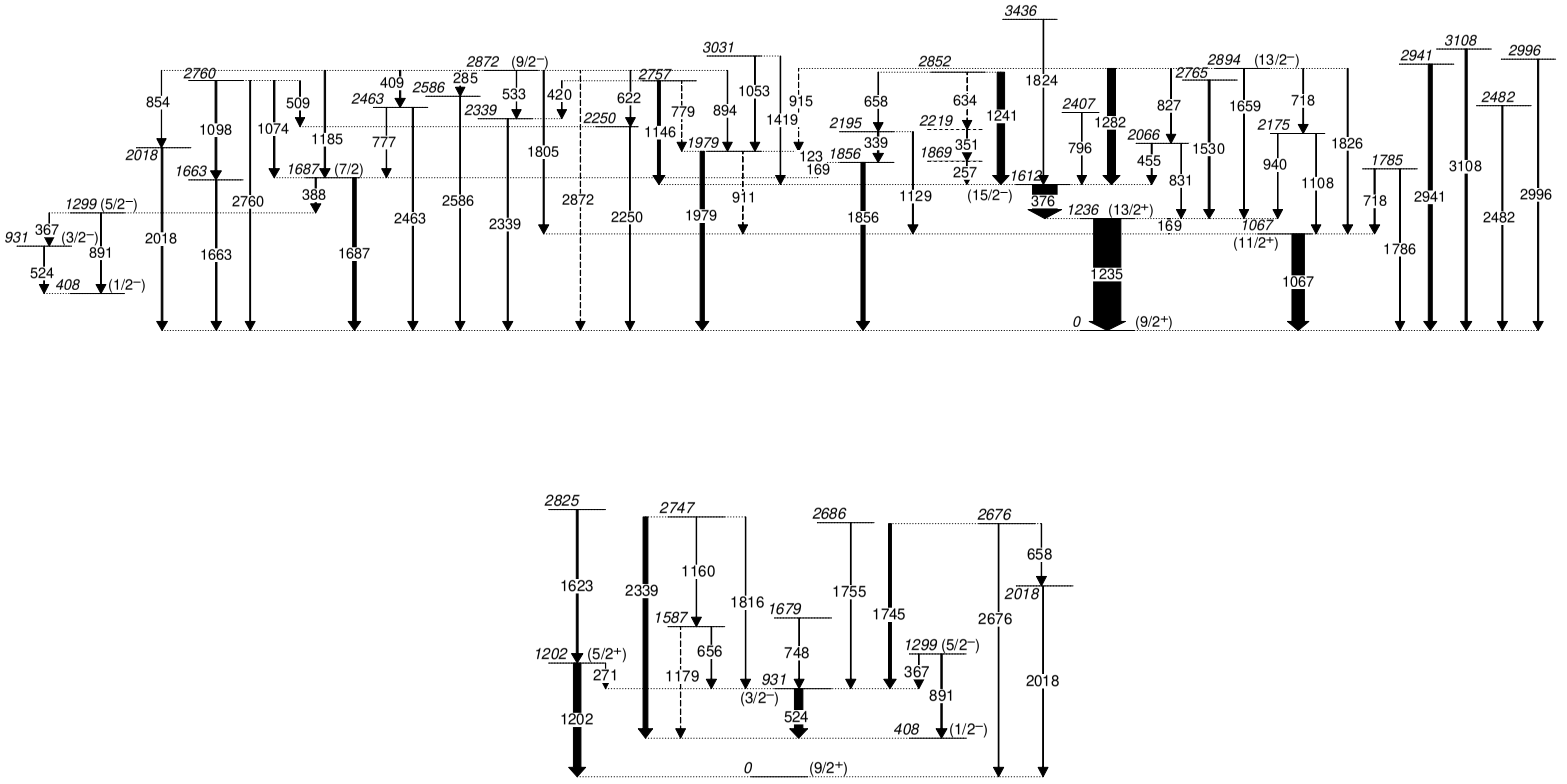


**Figure 6.3:** Decay scheme of $^{127}$In following the decay of the $11/2^-$ (top) and $3/2^-$ (top) state in $^{127}$Cd. Energy labels are in keV, tentative levels and transitions are dashed.

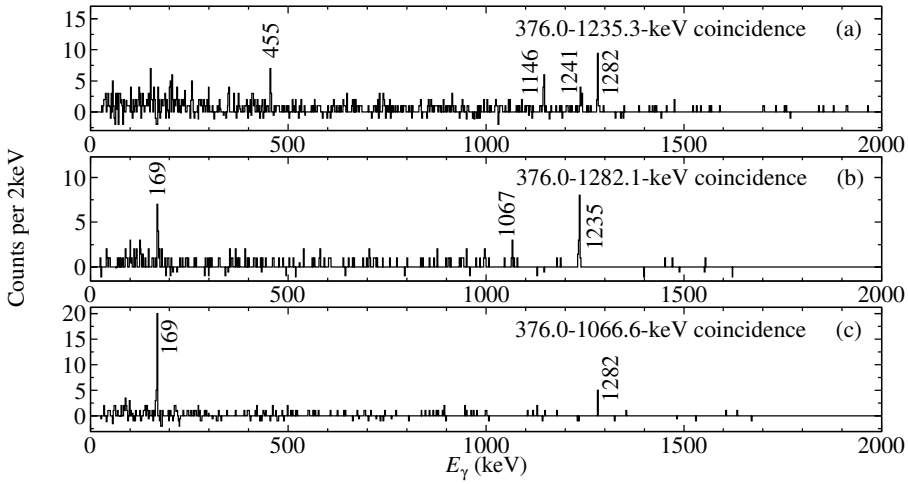


**Figure 6.4:** Observed $\gamma$-ray spectra in prompt coincidence with the 376 keV transition and the (a) 1235, (b) 1282, (c) 1067 keV transition. Energy labels are in keV.

Starting with these $\gamma$-ray transitions the decay scheme of $^{127}$In can be established by studying their prompt coincidence spectra, as discussed in great detail in Paper III section III A. Proposed decay schemes for the $\beta$ decay of the $11/2^-$ and $3/2^+$ state in $^{127}$In are shown in figure 6.3. The prominent structure around the 376 keV transition in the $\beta$ decay of the $11/2^-$ state, for instance, can be supported be investigating prompt $\beta$-$\gamma$-$\gamma$-$\gamma$ coincidence relations. Figure 6.4 shows the $\gamma$-ray spectrum in prompt coincidence with the 376 keV transition and either the 1067, 1235, or 1282 keV transitions. When requiring the 376 and 1282 keV transitions, i.e. following the $\gamma$ de-excitation through these two transitions, one observes only the three 169, 1067, and 1235 keV transitions, as shown in figure 6.4(b). Since the sum energy of the former two transition equals the energy of the 1235 keV transition, it appears natural to place them in parallel with the 1235 keV transition. This is supported by the fact that neither of the 169 or 1067 keV transitions is observed in prompt coincidence with the 1235 keV transition, which can be seen in figure 6.4(a). There, $\gamma$-ray peaks at 455, 1146, 1241, and 1282 keV are observed in prompt coincidence with both the 376 and 1235 keV transitions. Hence, they must be placed on top of the 376 keV transition, feeding the state at 1611 keV. The 1282 keV transition, which is the most intense peak in the 376-1235 keV coincidence spectrum, is also observed in the 376-1067 keV coincidence spectrum shown in figure 6.4(c). The second visible peak corresponds to the 169 keV transition, which links the 1067 and 1235 keV states.

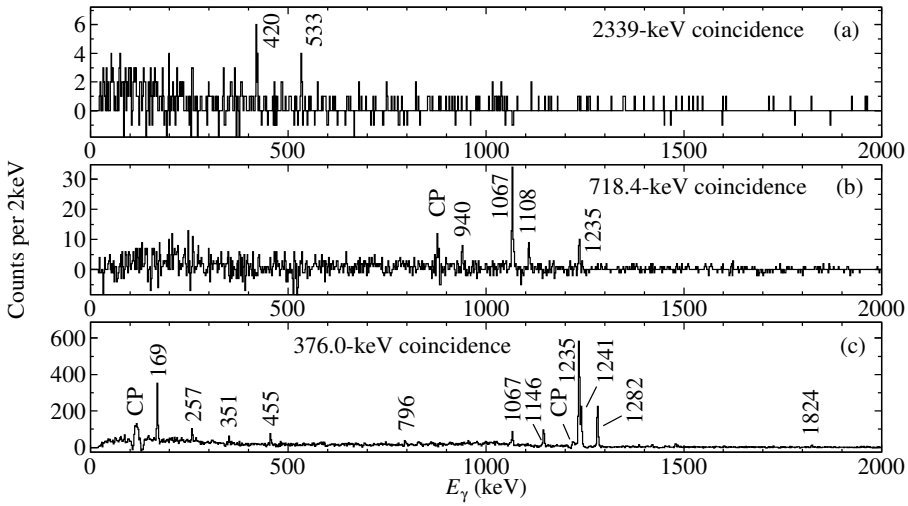


**Figure 6.5:** Observed $\gamma$-ray spectra in prompt coincidence with the (a) 2339 keV transition, the (b) 718 keV transition, and the (c) 376 keV transition. The latter spectrum is taken from Paper III and included for comparison of the relative peak intensity of the 1067 and 1235 keV in panel (b). Peaks marked (CP) stem from Compton scattered $\gamma$ rays of intense transitions with higher energies. For instance, the broad peak at 115 keV in panel (c) stems from a Compton scattered 491 keV $\gamma$ ray, which first deposited 115 keV (376 keV) in a Compton interaction and then via a full-absorption interaction in another HPGe crystal the remaining energy of 376 keV (115 keV).

Figure 6.5 shows the coincidence spectra of the 718 and 2339 keV doublets, which were also discussed in Paper III section III A.
The coincidence spectrum of the 2339 keV peak shows two $\gamma$-ray peaks at 420 and 533 keV. Since their sum energies can be identified with the states at 2757 and 2872 keV, respectively, it suggests a placement of the 2339 keV transition as a ground-state transition connected to the 2757 and 2872 keV states by the 420 and 533 keV transitions, respectively. A second possibility for placing this transition is a direct transition from the 2747 keV state to the $1/2^-$ isomer, as seen in figure 6.3. This placement is supported by the different intensity of the 2339 keV peak measured in this work, 23 %, compared to the intensity reported previously by Hoff *et al.* [80], 39 %. As it is pointed out in Paper III section III A 4, transitions which are populated during the $\beta$ decay of the $^{127}$Cd $11/2^-$ state are expected to be observed with the same relative intensity in this work as in the by Hoff *et al.* On the other hand, transitions following the $\beta$ decay of the $^{127}$Cd $3/2^+$ state are observed only with half of their previously reported intensity. Hence, the 2339 keV transition appears to be mainly populated by the $\beta$ decay of the $^{127}$Cd $3/2^+$ state. This fits the placement as a transition

de-exciting the 2747 keV state, which is a prime candidate for direct Gamow-Teller, and therefore strong, feeding from the $\beta$ decay of the $^{127}$Cd $3/2^+$ state. This is not the case for the 2339 keV state. Since it connects with the $9/2^-$ 2872 keV state and the $9/2^+$ ground-state, its spin must be larger than 5/2 assuming only fast $E1$, $M1$, and $E2$ transitions. This excludes direct Gamow-Teller feeding from the $\beta$ decay of the $^{127}$Cd $3/2^+$ state and one can assume that this state is only populated during the $\beta$ decay of the $^{127}$Cd $11/2^-$ state. Having the 2339 keV peak clearly divided into one part being populated by the $^{127}$Cd $3/2^+$ $\beta$ decay and the other part populated by the $^{127}$Cd $11/2^-$ $\beta$ decay, allows for an estimation of the individual transition intensities. Assuming the $3/2^+$ component to be just half as intense as in the experiment by Hoff *et al.* and the $11/2^-$ component equally intense, one can estimate the 2339 keV ground-state transition to have an intensity of 7.2(66) %. Accordingly, the intensity of the 2339 keV transition populating the isomer can be estimated to 16(5) %.

In figure 6.5(b) the spectrum in prompt coincidence with the 718 keV peak is shown. The proposed placement of the 940 and 1108 keV transitions, depopulating a state at 2175 keV, which in turn is connected to the well established 2894 keV state by the 718 keV transition (see figure 6.3), is clearly supported by the observation of $\gamma$-ray peaks at 940, 1067, 1108, and 1235 keV in figure 6.5(b). However, it cannot explain the comparably high yield of the 1067 keV peak. Following the de-excitation of the 2175 keV state by the 940 keV transition then one would expect the intensity ratio of the 1067 and 1235 keV peak to be about the same as in the prompt coincidence spectrum of the 376 keV transition, which is shown in figure 6.5(c). There the 1235 keV peak is much more pronounced than the 1067 keV peak, i.e. the 1235 keV state mostly de-excites directly to the ground state. Hence the de-excitation via the 940 keV transition does not contribute significantly to the 1067 keV peak in figure 6.5(b). On the other hand, if the 2175 keV state de-excites by the 1108 keV transition, then the 1067 keV peak in figure 6.5(b) should only be about the same intensity as the 1108 keV peak. Therefore, a second 718 keV transition is proposed, directly feeding into the 1067 keV state. This leads to a new state at 1785 keV, which is supported by the observation of a $\gamma$-ray peak with this energy in the measured total $\gamma$-ray spectrum (see Paper III figure 2).

In order to estimate the population of the $^{127}$In ground state and isomeric state by either direct $\beta$ feeding or unobserved $\gamma$ transitions from excited states the $\gamma$-ray peaks associated with the $\beta$ decay of $^{127}$In are investigated. The 1597 keV $\gamma$-ray transition, for instance, is a unique signature for the $\beta$ decay of the $^{127}$In ground state [22]. Since the absolute intensity, $I_\gamma$, of this transition is known, as well as the relative efficiency of the setup, $\epsilon_{rel}$ (see section 3.2.5), one can estim-

ate the relative number of $^{127}$In ground-state decays, $N_{rel}(^{127gs}In)$, according to equation 6.1, where $N_\gamma$ in this case is the number of detected 1597 keV photons. This can be repeated with other $\gamma$-ray transitions that are unique to the $^{127}$In ground-state decay and an average number can be calculated. A similar estimation can be carried out for the relative number of $^{127}$In isomer $\beta$-decays, $N_{rel}(^{127m}In)$. Thereby the relative population of the $^{127}$In isomer and $^{127}$In ground state can be estimated to $\frac{N_{rel}(^{127m}In)}{N_{rel}(^{127gs}In)} = 0.32(4)$.

$$N_{rel}(< nucleus >) = \frac{N_\gamma}{\epsilon_{rel}(E_\gamma) I_\gamma} \tag{6.1}$$

$$I_\gamma(^{127}\text{In}) = \frac{N_\gamma}{\epsilon_{rel}(E_\gamma)\left(N_{rel}(^{127gs}In) + N_{rel}(^{127m}In)\right)} \tag{6.2}$$

Furthermore, knowing $N_{rel}(^{127gs}In)$ and $N_{rel}(^{127m}In)$ makes it possible to estimate absolute intensities for the observed $\gamma$-ray transitions observed in $^{127}$In according to equation 6.2. Note that the relative efficiency is sufficient for these calculations and an absolute efficiency is not required.

## 6.2 The $^{127}$Cd $\beta$ decay

With the help of the absolute transition intensities of $\gamma$-ray transitions in $^{127}$In (see section 6.1) one can estimate the $\beta$ feeding into excited states, by calculating the balance of ingoing and outgoing $\gamma$-transition intensities for a state. For the ground state one obtains an absolute $\gamma$-ray feeding of 66(3) %, whereas we know that about 76(3) % of all $^{127}$In $\beta$ decays should be decays of the $^{127}$In ground state. Hence, 10(4) % of the feeding into the $^{127}$In ground state are either due to weak and therefore unobserved $\gamma$-ray transitions or due to direct $\beta$ feeding from a first-forbidden $\beta$ decay of the $11/2^-$ state in $^{127}$Cd. The corresponding number for the $1/2^-$ isomer in $^{127}$In is 12(3) %.
As described in Paper III section III B the majority of all the observed $\gamma$-ray transitions in $^{127}$In can be correlated to either the $\beta$ decay of the $11/2^-$ or the $3/2^+$ state in $^{127}$Cd. Together with the estimated $\beta$ feedings one can then calculate $log\ ft$ values characterizing the $\beta$ feeding into each state of $^{127}$In. Furthermore, it can be concluded that the $^{127}$Cd isomer corresponds to the $11/2^-$ state and the ground state to the $3/2^+$ state. These results are presented and discussed in Paper III section III B.
Having each state, and therefore each transition in $^{127}$In, associated with either the decay of the $11/2^-$ state or the $3/2^+$ state in $^{127}$Cd, allows for an individual half-life estimation of these two states. This was done by investigating the time

distribution of $\beta$ particles that are in prompt coincidence with $\gamma$ rays which have been found to be characteristic for the decay of one of the two states. For the $\beta$ decay of the $11/2^-$ state such $\gamma$-ray transitions are the 169, 376, 1067, 1146, 1235, 1241, and 1282 keV $\gamma$-ray transitions. Selecting only events involving these $\gamma$ rays and subtracting the Compton background for each of these $\gamma$-ray peaks leads to the blue time distribution shown in figure 6.6(a). This distribution can then be approximated with a single exponential function (see equation 2.1), resulting in a half-life of $T_{1/2} = 0.36(4)$ s for the $11/2^-$ state. With the same method a half-life of $T_{1/2} = 0.45(^{12}_{8})$ s can be obtained for the $3/2^+$ state (see red time distribution in figure 6.6(a)), based on the 524, 1202, 1623, and 1745 keV $\gamma$-ray transitions. As discussed in section 3.1.1 and seen in figure 3.6, only events which were detected $\sim 20$ ms after a trap release are suitable for this half-life analysis.

A slightly different method of determining these half-lives is to compare the peak areas of the characteristic $\gamma$ rays when detected in the time interval $T_1 = [20, 80]$ ms after a trap release to their peak area when detected in the time interval $T_2 = [80, 140]$ ms. Due to the exponential nature of nuclear decays, it can be shown, that the two areas $A_1$ and $A_2$ under the exponential decay curve as defined in equation 6.3 fulfill equation 6.4(a). In our case, $t_0 = 20$ ms and $\Delta t = 60$ ms. Filling two $\gamma$-ray spectra for the time interval $T_1$ and $T_2$, one can estimate the corresponding areas $A_1$ and $A_2$ by determining the peak area of a characteristic $\gamma$-ray peak in these two spectra. The decay constant can then be estimated via equation 6.4(b) and the half-life calculated using equation 2.1(b).

$$A_1 = \int_{t_0}^{t_0+\Delta t} A_0 \mathrm{e}^{-\lambda t}\,\mathrm{d}t \tag{6.3a}$$

$$A_2 = \int_{t_0+\Delta t}^{t_0+2\Delta t} A_0 \mathrm{e}^{-\lambda t}\,\mathrm{d}t \tag{6.3b}$$

$$\frac{A_1}{A_2} = \mathrm{e}^{\lambda \Delta t} \tag{6.4a}$$

$$\lambda = \frac{\ln \frac{A_1}{A_2}}{\Delta t} \tag{6.4b}$$

This approach leads to consistent and similar results as the exponential approximation of the time distribution in figure 6.6(a). Applying this method to the 376 keV peak a half-life of $0.34(^{6}_{4})$ s is obtained for the $\beta$ decay of the $11/2^-$ state. Adding up all $\gamma$-ray peaks that are characteristic for this decay, results in a half-life of $0.36(^{4}_{3})$ s, exactly the same as obtained in figure 6.6(a). Likewise, the resulting half-life for the $3/2^+$ state in $^{127}$Cd is $0.44(^{11}_{7})$ s.

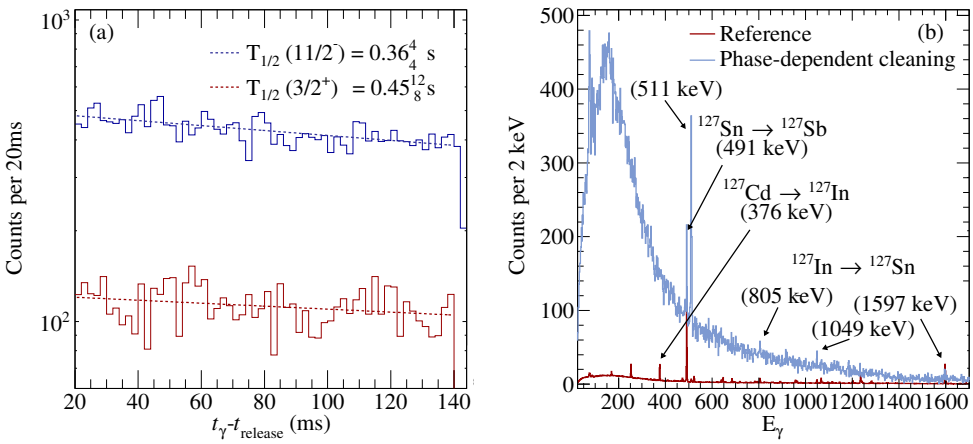


**Figure 6.6:** (a) Time distribution of $\beta$ particles which are in prompt coincidence with (blue) a 169, 376, 1067, 1146, 1235, 1241, or 1282 keV $\gamma$ ray, and (red) 524, 1202, 1623, or 1745 keV $\gamma$ ray. (b) $\gamma$-ray spectrum in prompt coincidence with a $\beta$ particle recorded (blue) employing the phase-dependent cleaning (PDC) method to individually study the decay of $^{127m}$Cd, and (red) without separating the $^{127}$Cd isomeric and ground state. The reference spectrum is normalized to the 491 keV peak of the PDC spectrum. Clearly visible $\gamma$-ray peaks from daughter decays in the PDC spectrum are indicated, as well as the most intense $\gamma$-ray peak observed in the reference spectrum.

## 6.3 Phase Dependent Cleaning of $^{127m}$Cd

As already mentioned in section 2.3.3, an attempt was made to separate the $^{127}$Cd grounds state and isomeric state by employing the phase-dependent cleaning (PDC) method [16]. Data has been recorded for 11 h with a trap cycle of 418 ms delivering $\sim$ 20 $^{127m}$Cd ions per minute. The recorded spectrum of $\gamma$ rays in coincidence with a $\beta$-particle is shown in figure 6.6(b). As a reference the $\gamma$-ray spectrum obtained in the 44h long $^{127}$Cd run without the separation of ground and isomeric state is shown as well, normalized to the intensity of the 491 keV peak.

The only clearly visible peaks in the $\gamma$-ray spectrum (besides the 511 keV annihilation peak) are at 491, 805, 1049 and 1597 keV. From the presence of only those peaks one can conclude that preferably the $^{127}$In ground state is populated after the decay of the delivered $^{127m}$Cd ions. This is in line with the suggested assignment of the $11/2^-$ state to the isomer and the $3/2^+$ state to be the ground state. Otherwise one would expect the $\beta$-decay of the $^{127}$Cd isomer to preferably populate the $1/2^-$ $^{127}$In isomer. From the decay of the $^{127}$In isomer

to $^{127}$Sn one would then expect a significant peak at 253 keV instead of the observed peaks at 805, 1049 and 1597 keV. However, no such peak is observed in the $\gamma$-ray spectrum when employing the PDC method.
When comparing to the reference spectrum, where a mixed beam of $^{127}$Cd ground state ($\approx 20\,\%$) and isomeric state ($\approx 80\,\%$) was delivered to TASISpec, one finds that the 376 keV appears to be absent in the PDC spectrum. Applying the ratio of the 491 keV $\gamma$-ray peak in the reference and PDC spectrum to the 376 keV peak, one obtains an estimated 376 keV peak intensity of about 53(13) counts in the PDC spectrum. This is, however, on the order of the statistical fluctuations and has therefore no statistical significance.

# Chapter 7

# Concluding Remarks

In this work, the high mass-resolving power of the Penning traps SHIPTRAP and JYFLTRAP was utilized to obtain isotopically pure beams of the $^{213}$Ra ground state and $^{127}$Cd, respectively. The decay of these nuclei were studied with the TASISpec decay station, which allows for charged-particle and photon detection as well as coincidence measurements.
The experimental results of the $^{213}$Ra experiment were confronted with detailed GEANT4-simulations, resembling the experimental conditions, the decay-path of $^{213}$Ra, and detection processes. Thereby, the $\alpha$-decay branching ratios of $^{213}$Ra to the ground and excited states of $^{209}$Rn were found to differ significantly from the hitherto reported values. The revised $\alpha$-decay branching ratios are supported by theoretical calculations. These discrepancies can be explained by the energy summing of $\alpha$ particles, conversion electrons and Auger electrons. This effect has substantial impact on the observed particle spectra, whenever an excited state, which is populated by an $\alpha$ decay, de-excites via highly converted transitions. Such decay patterns are rather common in heavy and super heavy nuclei, as was also pointed out in previous studies, e.g. [82, 83]. The magnitude of this effect suggests that published decay data of such nuclei should be reassessed in cases where summing effects were not – or could not be– considered in all aspects at the time.
It is important to note that the exclusive selection of the $^{213}$Ra ground state with SHIPTRAP, and hence the absolute knowledge about the beam composition, is crucial to perform meaningful and comparable 'virtual experiments' with GEANT4. The method of deducing decay properties by confronting experimental results with such simulations is inherently limited by the complexity of the decay schemes, i.e. the number of free parameters one has to vary in the simulation. For problems that are more complex than the studied $^{213}$Ra ground-

state decay, a fully automated framework is needed, which can autonomously start simulations, compare the result to the experimental observation, and suggest a new set of parameters for the next simulation. Such a framework is in development.
One disadvantage for $\alpha$-decay spectroscopy using this experimental scheme is the shallow implantation of the nuclei of interest in the DSSSD. This leads to worse resolution of the particle spectra because of dead-layer effects and does not allow for implantation-decay correlation. To achieve an implantation into the active detector material, one would need to post accelerate the ions of interest to some 20-30 MeV after they have been released from the Penning trap. Also experiments studying proton emitters such as the $^{53}$Co isomer would benefit from that. This, however, is a non-trivial and expensive task.
In the study of the $^{127}$Cd $\beta$ decay, the level scheme of $^{127}$In could be substantially extended, comprising 84 $\gamma$-ray transitions connecting 43 excited states. The $\beta$ decay feeding from the $\beta$ decay of the $3/2^+$ and $11/2^-$ states in $^{127}$Cd to the individual states of $^{127}$In has been estimated and $log\ ft$ values have been deduced. These findings were compared to extensive shell-model calculations with NuShellX@MSU, using the NA-14 interaction. Applying the calculated Gamow-Teller strength distribution, level energies as well as $\gamma$-ray branching ratios in $^{127}$In it is possible to reproduce the experimentally observed $^{127}$In decay scheme remarkably well. Hence, one can conclude that the $\beta$ decay of $^{127}$Cd is in fact predominantly driven by the $\nu g_{7/2} \rightarrow \pi g_{9/2}$ Gamow-Teller transition, since it is the only allowed Gamow-Teller transition in the considered shell-model space. However, the deduced upper limit on $\beta$ feeding to the $9/2^+$ ground state and the $1/2^-$ isomeric state do not exclude first-forbidden transitions.
Despite not being measured separately, the $3/2^+$ and $11/2^-$ $\beta$ decaying states in $^{127}$Cd could be identified as the ground state and the 283 keV isomer. This is in line with the predictions of the conducted shell-model calculations, which suggest a crossing of the $3/2^+$ and $11/2^-$ states for $^{129}$Cd. The effort has been taken to employ the new phase-dependent cleaning method in order to separate the $^{127}$Cd isomer from the ground state and study its decay independently. It was possible to obtain some spectroscopic information which, unfortunately, did not yield enough statistics to draw significant conclusions. Here a limiting factor was the saturation of the Penning trap due to other isobars dominating the beam by far. In order to reduce the ratio of isobaric contaminants in the beam before the beam reaches the Penning trap, a Multi-Reflection Time-of-Flight (MR-ToF) spectrometer is currently being installed at the IGISOL facility at the University of Jyväskylä. With this additional stage the cleaning with the Penning trap can be conducted much more efficiently.
As mentioned earlier, an implantation of the $\beta$-decaying nuclei into the active detector volume would be very advantageous, too. On the one hand, the $\beta$ particles

are not as significantly affected by the dead layer as the much heavier protons and $\alpha$ particles. But on the other hand, by using implantation-decay correlation one could improve the separation between the decays of the mother and each daughter nucleus. Hence, characteristic photon spectra could be measured for each individual nucleus involved in the decay chain. In contrast to proton and $\alpha$ spectroscopy, where the detected charged particles have discrete energies, this cannot be achieved by dedicated $\beta$-$\gamma$ coincidence correlations, because of the continuous energy spectrum of the $\beta$ particles. Furthermore, depending on their kinetic energy, $\beta$ particles deposit just a fraction of their energy in the DSSSDs.

Another possibility to suppress daughter activity is a tape system. In that case the ion beam is not implanted directly in the detector or a fixed catcher foil, as it was the case in the $^{127}$Cd experiment, but on a tape, which transports the implanted ions to the decay station in regular intervals. Thereby, the daughter activity is removed with every interval and a fresh sample of the nuclei of interest is moved into the decay station. Using a tape system would also improve on the effect of the dead layer on the energy resolution if proton and $\alpha$ decaying nuclei are studied. Positioning the tape system such that the decaying nuclei are in the centre of the TASISpec silicon-detector cube leads to much less angular spread with which the proton and $\alpha$ particles have to traverse the dead layer in order to reach the active detector volume, compared to the shallow implantation in the detector without post acceleration. Hence, the resolution is improved.

Additionally, the quality of the photon spectra can be improved by employing Anti Compton Shields (ACS) for each of the HPGe detectors. Due to the very close and cube-like arrangement of the HPGe detectors, the probability of detecting a photon, that underwent Compton scattering in one crystal, with one of the other crystals is rather high. This, for instance, can lead to unwanted contributions in $\gamma$-$\gamma$ correlation matrices. With an ACS one would suppress this effect to a large extend. Furthermore, an ACS could actively shield the detectors from ambient background radiation, which was very prominent in the experimental hall of the IGISOL facility at the University of Jyväskylä.

# Appendix A

# Input for NuShellX@MSU calculations of $^{127}$Cd and $^{127}$In

To calculate shell-model based nuclear wave functions and energy levels for the ground and excited states of $^{127}$Cd and $^{127}$In in the NuShellX@MSU framework, the `shell` command has to be called with the following input file:

```
Cd127-In127WF.in
-------------------------
Cd127-In127WF    ! name of the produced batch file
lpe,2            ! option for wave function calculation
jj45pn           ! model space
n                ! no restrictions
CSn210           ! interaction (corresponds to NA-14)
49               ! number of protons (127In)
127              ! number of nucleons
0.5,20.5         ! range of spins J to be calculated
2                ! calculate pos. and neg. party states
lpe,2            ! next calculation for 127Cd
48               ! number of protons (127Cd)
127
0.5,21.5
2
st               ! stop
-------------------------
```

Calling `shell < Cd127-In127WF.in` will produce a number of ancillary files and a batch file `Cd127-In127WF.bat`. When running this batch file, NuShellX@MSU will calculate the desired wave functions and energy levels.
The energy levels and the name of the corresponding wave functions are listed in the `in27h.lpt` and `cd27h.lpt` files. For each spin-party $J^\pi$ one `*.lp` file is created containing the average occupation numbers of the considered orbitals and the individual contributions of the single-particle wave functions for all states with spin-parity $J^\pi$.
By default, at maximum ten levels for each spin and parity are calculated. This can be modified by creating a `neig.dat` file prior to calling `shell` containing the desired value. Alternatively, one can modify the desired number of states for each $J^\pi$ individually in the `*.neig` files, which are produced alongside the batch file after `shell` has been called.
Once these wave functions have been calculated, reduced transitions probabilities for $\gamma$-ray transitions can be calculated. Using the following input file for the `shell` command produces the necessary files for $^{127}$In:

```
In127gamma.in:
-------------------------
in127            ! name of the produced batch file
den              ! option to calculate wavefunction overlaps
t                ! the one-body transition density overlap option
rhlN00           ! name of initial states (127In pos. parity)
20               ! number of initial states
rhlN00           ! name of final states (127In pos. parity)
20               ! number of final states
0.5,9.5          ! range of spins J for initial states
0.5,9.5          ! range of spins J for final states
y                ! restrict tensor ranks for the one-body operator
1.,2.            ! min, max tensor-rank (here for E1, M1, E2, M2)
den              ! next calculation
t
rhlN00           ! name of final states (127In pos. parity)
20
rhlN10           ! name of final states (127In neg. parity)
20
0.5,9.5
0.5,9.5
y
1.,2.
den              ! next calculation
```

```
t
rhlN10           ! name of final states (127In neg. parity)
20
rhlN00           ! name of final states (127In pos. parity)
20
0.5,9.5
0.5,9.5
y
1.,2.
den              ! next calculation
t
rhlN10           ! name of final states (127In neg. parity)
20
rhlN10           ! name of final states (127In neg. parity)
20
0.5,9.5
0.5,9.5
y
1.,2.
st               ! stop
-------------------------
```

Running the newly created `In127.bat` file starts the calculations. The results are stored in `in270h.deo` and `in271h.deo`. In the corresponding `*.den` files the default effective charges and free $g$-factors values can be modified prior to calling `In127.bat`.
Similarly the Gamow-Teller strength distribution can be calculated. Using again the `shell` command the following two input files are used to prepare the calculations for the allowed $\beta$ decays of the $^{127}$Cd $11/2^-$ and $3/2^+$ states:

```
Cd127-In127-GT11.in
-------------------------
Cd127-In127-GT11 ! name of the produced batch file
den              ! option to calculate wavefunction overlaps
t                ! the one-body transition density overlap option
rhkN1            ! name of initial states (127Cd neg. parity)
1                ! number of initial states (just the first state)
rhlN1            ! name of final states (127In neg. parity)
20               ! number of final states
5.5              ! range of spins J for initial states (only 11/2)
4.5,6.5          ! range of spins J for final states (9/2 to 13/2)
```

```
n                ! restrict tensor ranks for the one-body operator
st               ! stop
-------------------------
```

```
Cd127-In127-GT3.in
-------------------------
Cd127-In127-GT3  ! name of the produced batch file
den              ! option to calculate wavefunction overlaps
t                ! the one-body transition density overlap option
rhkN0            ! name of initial states (127Cd pos. parity)
1                ! number of initial states (just the first state)
rhlN0            ! name of final states (127In pos. parity)
20               ! number of final states
1.5              ! range of spins J for initial states (only 3/2)
0.5,2.5          ! range of spins J for final states (1/2 to 5/2)
n                ! restrict tensor ranks for the one-body operator
st               ! stop
-------------------------
```

The respective `shell` calls should be done in separate directories to avoid overwriting each others files. Thereafter, one can modify the $Q_\beta$ value and the quenching factor in the newly created `*.beq` files.
The default value for the quenching factor is 0.60 and has been changed to 0.75 for the calculations [84, 85]. Furthermore, it is important to note that in these calculations NuShellX@MSU treats the energetically lowest allowed final state as the ground state. For example, in the calculations for the GT strength distribution of the $^{127}$Cd $3/2^+$ ground state, the 1202 keV $5/2^+$ state is treated as the ground state, and the $Q_\beta$ value should be corrected for that. Instead of using the ground-state to ground-state $Q_\beta$ value of $Q_\beta = 8149\,\text{keV}$ [86], one should explicitly enter $Q_\beta = 8149\,\text{keV} - 1202\,\text{keV} = 6947\,\text{keV}$ as $Q_\beta$ value. Similarly, the excitation energy of the $^{127}$Cd $11/2^-$ isomer at 283 keV has to be taken into account. There the first allowed final state is calculated to be at 1889 keV, which can be identified with the experimentally observed state at 1856 keV. Hence the entered value should be $Q_\beta = 8149\,\text{keV} - 1856\,\text{keV} + 283\,\text{keV} = 6576\,\text{keV}$. After modifying these values and running the batch file, the resulting GT strength distributions are stored in the `cd27mh.beo` files.

# References


[1] E. Rutherford, The London, Edinburgh, and Dublin Philosophical Magazine and Journal of Science **21**, 669 (1911).

[2] R. F. Casten, *Nuclear structure from a simple perspective* (Oxford University Press, 2005).

[3] K. S. Krane, *Introductory Nuclear Physics* (John Wiley & Sons, New York, 1998).

[4] D. S. Delion, *Theory of Particle and Cluster Emission* (Springer, Berlin, Heidelberg, 2010).

[5] H. Horiuchi, K. Ikeda, and K. Katō, Prog. Theo. Phys. Supp. **192**, 1 (2012).

[6] T. Suzuki et al., Phys. Rev. Lett. **75**, 3241 (1995).

[7] G. Audi, F. G. Kondev, M. Wang, W. J. Huang, and S. Naimi, Chin. Phys. C **41**, 030001 (2017).

[8] S. Agostinelli et al., Nucl. Instrum. Methods Phys. Res., Sect. A **506**, 250 (2003).

[9] J. Allison et al., Nucl. Instrum. Methods Phys. Res., Sect. A **835**, 186 (2016).

[10] P. Spädtke et al., Nucl. Instrum. Methods Phys. Res., Sect. B **139**, 145 (1998).

[11] G. Münzenberg et al., Nucl. Instrum. Methods **161**, 65 (1979).

[12] M. Block et al., Eur. Phys. J. D **45**, 39 (2007).

[13] V. Kolhinen et al., Nucl. Instrum. Methods Phys. Res., Sect. B **317**, 506 (2013).

[14] I. Moore et al., Nucl. Instrum. Methods Phys. Res., Sect. B **317**, 208 (2013).

[15] T. Eronen et al., Eur. Phys. J. A **48**, 46 (2012).

[16] D. A. Nesterenko et al., Eur. Phys. J. A **54**, 154 (2018).

[17] S. Eliseev et al., Phys. Rev. Lett. **110**, 082501 (2013).

[18] G. Savard et al., Phys. Lett. A **158**, 247 (1991).

[19] S. George et al., Int. J. Mass Spectrom. **264**, 110 (2007).

[20] M. Block, *private communication.*

[21] J. Katakura, Nucl. Data Sheets **112**, 495 (2011).

[22] A. Hashizume, Nucl. Data Sheets **112**, 1647 (2011).

[23] L.-L. Andersson et al., Nucl. Instrum. Methods Phys. Res., Sect. A **622**, 164 (2010).

[24] J. Eberth et al., Prog. Part. Nucl. Phys. **28**, 495 (1992).

[25] J. Eberth et al., Nucl. Instrum. Methods Phys. Res., Sect. A **369**, 135 (1996).

[26] J. Gerl, H. Grawe, E. Roeckl, and H. Wollersheim, GSI Darmstadt, Report (1998).

[27] R. Page et al., Nucl. Instrum. Methods Phys. Res., Sect. B **204**, 634 (2003).

[28] J. Hoffmann et al., GSI Scientific Report **2012-1**, 253 (2012), GSI Annual Report.

[29] J. Adamczewski et al., IEEE Trans. Nucl. Sci. **51**, 565 (2004).

[30] R. Brun and F. Rademakers, Nucl. Instrum. Methods Phys. Res., Sect. A **389**, 81 (1997).

[31] I. Antcheva et al., Comp. Phys. Comm. **180**, 2499 (2009).

[32] H. G. Essel and N. Kurz, IEEE Trans. Nucl. Sci. **47**, 337 (2000).

[33] U. Forsberg, Ph.D. thesis, Lund University (2016).

[34] J. Stein, F. Scheuer, W. Gast, and A. Georgiev, Nucl. Instrum. Methods Phys. Res., Sect. B **113**, 141 (1996).

[35] D. Radford, Nucl. Instrum. Methods Phys. Res., Sect. A **361**, 297 (1995).

[36] T. Otsuka, *Shell Structure of Exotic Nuclei* (Springer Berlin Heidelberg, 2009), pp. 1–25, ISBN 978-3-540-85839-3.

[37] I. Talmi, *Simple Models of Complex Nuclei*, vol. 7 (Harwood Academic Publishers, 1993), ISBN 3-7186-0550-3.

[38] B. Rubio and W. Gelletly, *Beta Decay of Exotic Nuclei* (Springer Berlin Heidelberg, 2009), pp. 99–151, ISBN 978-3-540-85839-3.

[39] M. G. Mayer, Phys. Rev. **74**, 235 (1948).

[40] R. D. Woods and D. S. Saxon, Phys. Rev. **95**, 577 (1954).

[41] N. Lalović, Ph.D. thesis, Lund University (2017).

[42] M. G. Mayer, Phys. Rev. **75**, 1969 (1949).

[43] B. A. Brown, Prog. Part. Nucl. Phys. **47**, 517 (2001).

[44] B. A. Brown and W. D. M. Rae, Nucl. Data Sheets **120**, 115 (2014).

[45] B. A. Brown, W. D. M. Rae, E. McDonald, and M. Horoi, *NuShellX@MSU* (2018), https://people.nscl.msu.edu/~brown/resources/resources.html.

[46] N. A. F. M. Poppelier and P. W. M. Glaudemans, Z. Phys. A **329**, 275 (1988).

[47] L. Coraggio, A. Covello, A. Gargano, N. Itaco, and T. T. S. Kuo, Prog. Part. Nucl. Phys. **62**, 135 (2009).

[48] J. Taprogge et al., Phys. Lett. B **738**, 223 (2014).

[49] J. Taprogge et al., Phys. Rev. C **91**, 054324 (2015).

[50] J. Taprogge et al., Phys. Rev. Lett. **112**, 132501 (2014).

[51] J. Taprogge et al., Phys. Rev. Lett. **113**, 049902 (2014).

[52] A. Jungclaus et al., Phys. Lett. B **772**, 483 (2017).

[53] T. Kibédi, T. W. Burrows, M. B. Trzhaskovskaya, P. M. Davidson, and C. W. Nestor, Nucl. Instrum. Methods Phys. Res., Sect. A **589**, 202 (2008).

[54] T. Kibédi, T. W. Burrows, M. B. Trzhaskovskaya, P. M. Davidson, and C. W. Nestor, *BrIcc v2.3S* (The Australian National University, 2018), http://bricc.anu.edu.au.

[55] E. Fermi, Z. Phys. **88**, 161 (1934).

[56] G. Gamow and E. Teller, Phys. Rev. **49**, 895 (1936).

[57] M. Emeric and A. Sonzogni, *LOGFT* (NNDC, Brookhaven National Laboratory, 2018), https://www.nndc.bnl.gov/logft.

[58] L. Sarmiento, L.-L. Andersson, and D. Rudolph, Nucl. Instrum. Methods Phys. Res., Sect. A **667**, 26 (2012).

[59] D. Rudolph et al., Phys. Rev. Lett. **111**, 112502 (2013).

[60] D. Rudolph et al., Acta Phys. Pol. B **45**, 263 (2014).

[61] L. G. Sarmiento, D. Rudolph, U. Forsberg, P. Golubev, and L. L. Andersson, PoS **(X LASNPA)**, 057 (2014).

[62] D. Rudolph, L. G. Sarmiento, and U. Forsberg, AIP Conference Proceedings **1681**, 030015 (2015).

[63] D. Rudolph, U. Forsberg, L. Sarmiento, P. Golubev, and C. Fahlander, Eur. Phys. J. Web of Conferences **117**, 01001 (2016).

[64] U. Forsberg et al., Nucl. Phys. A **953**, 117 (2016).

[65] L. G. Sarmiento and D. Rudolph, AIP Conference Proceedings **1753**, 070007 (2016).

[66] S. Pommé and G. Sibbens, Acta Chim. Slov. **55**, 111 (2008).

[67] N. Gagunashvili, PoS **(ACAT)**, 060 (2009).

[68] M. Basunia, Nucl. Data Sheets **108**, 633 (2007).

[69] J. Chen and F. Kondev, Nucl. Data Sheets **126**, 373 (2015).

[70] F. Kondev, Nucl. Data Sheets **101**, 521 (2004).

[71] J. F. Ziegler, M. Ziegler, and J. Biersack, Nucl. Instrum. Methods Phys. Res., Sect. B **268**, 1818 (2010).

[72] D. E. Ward, B. G. Carlsson, and S. Åberg, Phys. Rev. C **88**, 064316 (2013).

[73] D. Ward, Ph.D. thesis, Lund University (2017).

[74] F. Kondev and S. Lalkovski, Nucl. Data Sheets **112**, 707 (2011).

[75] B. Singh et al., Nucl. Data Sheets **114**, 661 (2013).

[76] B. Singh et al., Nucl. Data Sheets **114**, 2023 (2013).

[77] D. T. Yordanov et al., Phys. Rev. Lett. **110**, 192501 (2013).

[78] S. Ohya, Nucl. Data Sheets **111**, 1619 (2010).

[79] S. Ohya, Nucl. Data Sheets **102**, 547 (2004).

[80] P. Hoff, B. Ekström, H. Göktürk, and B. Fogelberg, Nucl. Phys. A **459**, 35 (1986).

[81] O. Arndt et al., Acta Phys. Pol. B **40**, 437 (2009).

[82] F. P. Heßberger et al., Nucl. Instrum. Methods Phys. Res., Sect. A **274**, 522 (1989).

[83] F. P. Heßberger et al., Eur. Phys. J. A **8**, 521 (2000).

[84] C. B. Hinke et al., Nature (London) **486**, 341 (2012).

[85] E. Caurier, G. Martínez-Pinedo, F. Nowacki, A. Poves, and A. P. Zuker, Rev. Mod. Phys. **77**, 427 (2005).

[86] M. Wang et al., Chin. Phys. C **41**, 030003 (2017).

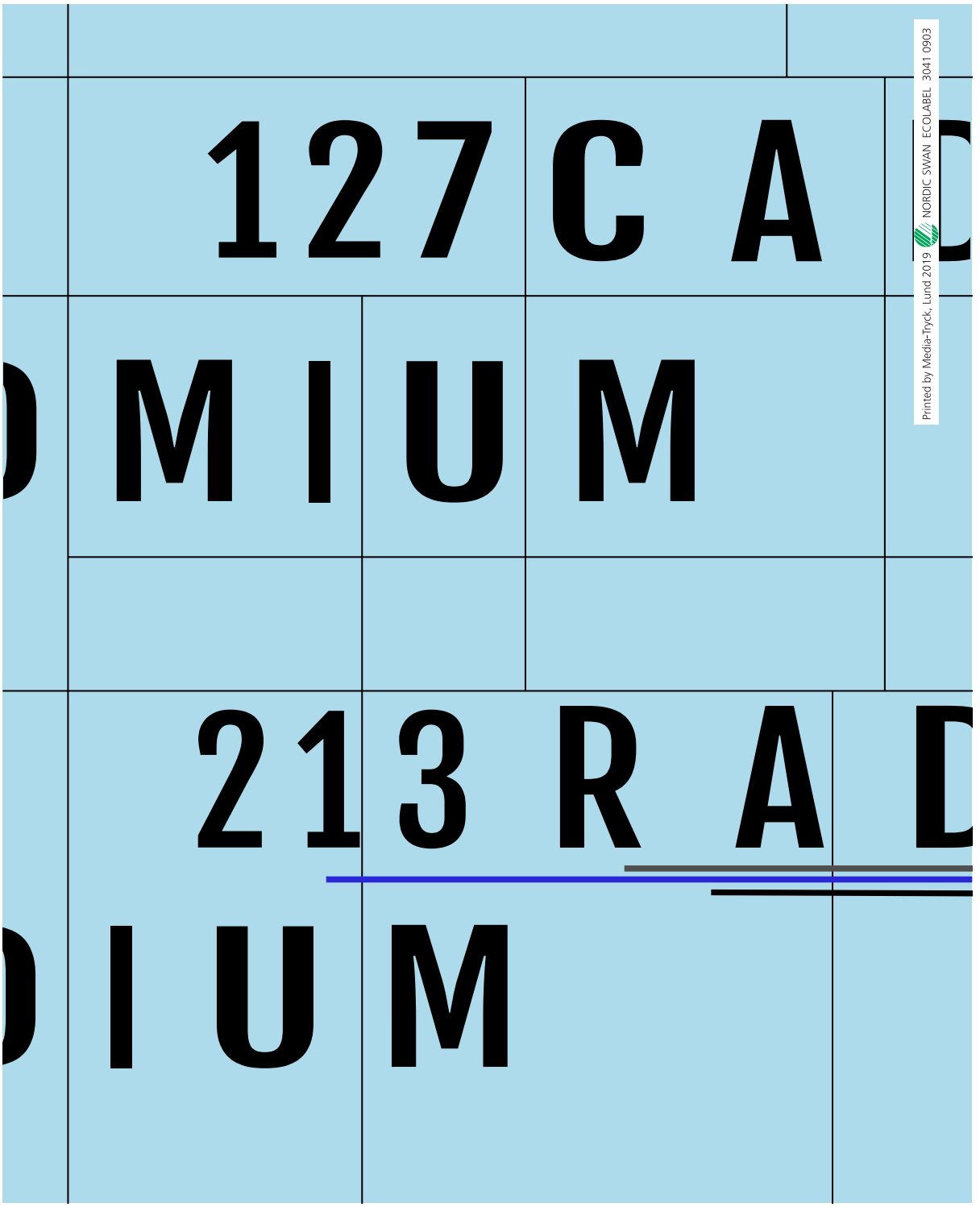


Printed by Media-Tryck, Lund 2019 NORDIC SWAN ECOLABEL 3041 0903

LUND UNIVERSITY

Faculty of Science
Department of Physics

ISBN 978-91-7753-942-1 (print)
ISBN 978-91-7753-943-8 (pdf)
ISSN LUNFD6/(NFFR-1043)/1-75(2019)